UNIVERSITY OF CAPE TOWN
IYUNIVESITHI YASEKAPA • UNIVERSITEIT VAN KAAPSTAD

The modelling of natural fibre-reinforced composites using a multi-scale methodology

by

Helen Lorna Morrissey

Thesis Presented in partial fulfillment
for the Degree of
MASTER OF SCIENCE IN ENGINEERING
in the Department of Mechanical Engineering
UNIVERSITY OF CAPE TOWN
July 2010

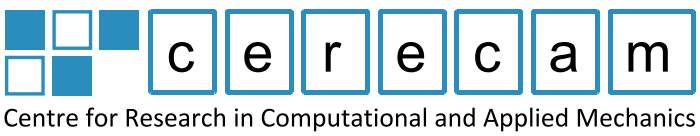

Plagiarism declaration

I know the meaning of plagiarism and declare that all of the work in the document, save for that which is properly acknowledged, is my own.

Signed: . . . . . .

Date:

The modelling of natural fibre-reinforced composites using a multi-scale methodology

Helen Lorna Morrissey
University of Cape Town

Abstract

A multi-scale methodology for small strain linear elasticity is presented in this thesis. The homogenisation process is discussed in general, with particular attention to the required boundary constraints on the micro-domain and the extraction of an effective elastic modulus. For the case of a non-linear problem the enforcement of the required boundary constraints becomes non-trivial and thus implementation via the penalty method and lagrange multipliers is investigated.

The microstructure in question involves needle-punched flax fibres bonded into a polymer matrix. This material comprises the outer layers of a laminated composite to be used for the interior componentry in aircraft. The inclusion of flax fibres, as opposed to a synthetic option, is desirable as it increases the number of recyclable components of an aircraft. The nature of the needlepunched fibres is such that the microstructure is random and the material is assumed to be macroscopically isotropic. The assumption of linear elasticity allows reduced computational labour as the entire analysis can be done at the micro-scale. These aspects lend themselves to the method presented by Zohdi and Wriggers [31], which was developed for spherical inclusions in a matrix, but is adaptable to the problem of long, thin fibres within a matrix.

The linear displacement boundary condition gives an upper bound on the stiffness for a random microstructure, and is thus implemented for the microstructure described. The domain is partitioned into subdomains and an individual boundary value problem is solved on each so that statistical analysis may be carried out on the data. The classical Reuss and Voigt bounds are derived and used in bounding the results of the analysis.

The finite element method is presented for small strain linear elasticity as it is used to solve the system of partial differential equations governing the problem on the micro-domain. The random geometry is generated via an algorithm developed in the Matlab programming language. The geometry is incorporated into a finite element model in Abaqus via Python script developed for the thesis. One of the important aspects in multi-scale modelling is the correct sizing of the RVE and, as such, various sized RVEs are tested.

The statistical arrays for different sized RVEs give similar mean values for all RVE sizes implemented. However the standard deviation for the larger samples is lower than that for the small samples. This means that the data for the individual subdomains is more accurate for larger RVE sizes. All subdomains give values lying within the theoretical bounds discussed, and the method is seen as successful, however there are various ways in which to improve the model, and these are discussed.

Acknowledgements

I must thank my supervisor, Professor Daya Reddy, for his excellent guidance throughout this thesis. My co-supervisor, Dr Andrew McBride, has been tireless in his assistance and support, even when it has been long-distance. Thanks also go to Hellmut Bowles from Abaqus, for all of his assistance, in particular for the Python script which he developed. I am also grateful to everyone in the CERECAM lab at UCT, including those that have left since I commenced my Master's degree, and those who have arrived during the process; here I have found a strange mix of friendship and academic guidance and advice. My erratic work schedule has demanded a high degree of patience from all of my friends and family, as well as a lot of love and care, and for this I am extremely grateful.

Contents

1 Introduction 1
- 1.1 Motivation and background 1
- 1.2 Objectives and limitations 4
- 1.3 Approaches to micro-macro modelling 5
- 1.4 Outline of thesis 9

2 Micro-macro modelling 11
- 2.1 Overview of classical continuum mechanics 11
  - 2.1.1 Infinitesimal strain 11
  - 2.1.2 Stress and the balance of linear and angular momentum 13
  - 2.1.3 Boundary conditions 14
  - 2.1.4 Linear elasticity 15
  - 2.1.5 The weak formulation 19
  - 2.1.6 Voigt notation 20
- 2.2 Homogenisation theory 21
- 2.3 Boundary condition enforcement on the RVE 24
  - 2.3.1 Lagrange multipliers 24
  - 2.3.2 Penalty method 26
- 2.4 Determining the elastic modulus 27
  - 2.4.1 Bounding the results: The Reuss and Voigt bounds 29
- 2.5 Partitioning of domain/bounding results 31
  - 2.5.1 Proof of Equations (2.61) to (2.63) 32

3 The finite element method . . . 37
3.1 The finite element method for small strain linear elasticity . . . 37
3.1.1 Implementing the finite element method . . . 39
3.2 Implementation of boundary condition enforcements . . . 45
3.2.1 Lagrange multipliers . . . 45
3.2.2 The penalty method . . . 48
3.2.3 Results of the investigation . . . 50

4 Testing methodology and implementation . . . 55
4.1 Calculation of elastic moduli with the assumption of isotropy . . . 55
4.2 Optimal RVE sizing and sampling . . . 56
4.2.1 Sizing the RVE . . . 57
4.3 Partitioning the domain . . . 57
4.4 Approximation to microstructure . . . 58
4.5 Generation of randomly orientated fibres . . . 59
4.6 Finite element implementation . . . 61
4.6.1 Modelling the material . . . 61
4.6.2 Postprocessing of results . . . 62
4.6.3 Expected distribution of data . . . 66

5 Results . . . 69
5.1 Sizing the RVE . . . 69
5.2 Simulations involving varying macro-RVE sizes . . . 70
5.3 Simulations involving varying fibre volume fractions . . . 74
5.3.1 Summary of results for final 30% volume fraction model . . . 74
5.4 Discussion . . . 76

6 Conclusions and recommendations . . . 79
6.1 Further tests . . . 79
6.1.1 Standard laboratory tests . . . 80
6.1.2 Investigating an anisotropic material . . . 80
6.2 Improvements in approximation to material structure . . . 81

6.2.1 Fibre geometry and modelling 81
6.2.2 Embedding the fibres 81
6.3 Material components and geometric nonlinearity 82

References 83

List of Figures

1.1 Examples of unprocessed natural fibres (Image courtesy of CSIR, Pretoria) 2
1.2 The entangled fibres post needlepunching process 3
1.3 The fibre-matrix composite bonded and used as the outer layers of a laminate. (image courtesy of the CSIR, Port Elizabeth) 3

2.1 Current and undeformed configurations of an arbitrary material body (image courtesy of [22]) 12
2.2 A specimen in a state of uniaxial stress 17
2.3 A specimen under hydrostatic pressure 18
2.4 A specimen in shear 19
2.5 The macro-scopic domain with magnified heterogeneous structure of microdomain 22
2.6 The boundary conditions on the micro-domain which satisfy Hill's condition 23
2.7 RVE with positive (+) boundaries and corresponding negative (-) boundaries 25
2.8 The partitioning of a "large" domain into 125 subdomains 32

3.1 Finite element meshes with a) nodes only at vertices and b) additional nodes 40
3.2 The shape function N_9 for global node number 9 41
3.3 Finite element mesh using a piecewise-linear approximation 42

3.4 The eight noded brick isoparametric element and the corresponding reference element 43
3.5 Meshed RVE with positive (+) boundaries and corresponding negative (-) boundaries 45
3.6 Homogeneous square, square with central hole and square with eccentric hole used in investigation of boundary condition constraints . . 50
3.7 Results using the lagrange multiplier method to enforce the periodic boundary constraint 52
3.8 Results using the penalty method to enforce the linear displacement boundary constraint 53

4.1 The relationship between the dimensions of the macro-domain, the RVE and the heterogeneities [28] 57
4.2 The procedure used to size the RVE. A small sample is used and the size is increased until the results become satisfactory 58
4.3 Scanning electron microscope image of material after bonding (Image courtesy of CSIR, Port Elizabeth) 59
4.4 Random fibre generation 61
4.5 The finite element mesh for the RVE 63
4.6 Resolving stress components 66

5.1 Scanning electron microscope image used in initial guess for sizing RVE 70
5.2 Effective material properties for 1cm macro-RVE 71
5.3 Effective properties for 0.75cm macro-RVE 71
5.4 Effective properties for 0.5cm macro-RVE 72
5.5 Effective properties for 0.25cm macro-RVE 72
5.6 Effective material properties for 0.125cm macro-RVE 73
5.7 Effective properties with increasing fibre volume fraction 75

List of Tables

3.1 Position of Gauss points and corresponding weights 44

4.1 Transformed fibre stresses 65

5.1 Results for RVEs of varying sizes 73
5.2 Results for RVEs of varying volume fraction 74
5.3 Ratio of standard deviation to mean values 74
5.4 Results for RVEs of varying volume fraction 76

1

Introduction

1.1 Motivation and background

Approximately 6000 aeroplanes will be retired over the next two decades, creating a number of waste disposal issues. Currently over 80% of any aircraft is recyclable, owing to the aluminium components in the fuselage; however, the interior componentry of these aircraft is still largely made up of non-recyclable, synthetic materials. An effective way in which to cut down on the waste materials in the disposal of old aircraft is to replace the use of synthetics with recyclable materials in the interior componentry. Natural fibres, abundant in South Africa, are potentially suitable, recyclable substitutes for synthetic materials and are being investigated as reinforcements in the fibre-reinforced laminated composites. This thesis aims to create a numerical model of the material, using a micro-macro modelling technique. Examples of various natural fibres in their unprocessed state are shown in Figure 1.1. [1].

The computational modelling of materials allows an understanding of the effects of various design parameters of a material. Experimental testing can be expensive and limiting with regard to the level of real-world situations which can be reproduced in a

[1] This project is in collaboration with the Council for Scientific and Industrial Research (CSIR), and forms part of an overarching project *Natfibio: Development of a natural fibre/bio-composite cabin interior component*, sponsored jointly by Airbus, the Department of Science and Technology, and the Advanced Manufacturing Technology Strategy.

Fig. 1.1: Examples of unprocessed natural fibres (Image courtesy of CSIR, Pretoria)

testing environment. Using computational modelling as a complement to experimental testing allows a greater understanding of the material in question as well as the opportunity to verify models using experimental data.

The natural fibre-matrix composite in question is heterogeneous and, as such, has varying physical properties throughout its microstructure. Many effects of the reinforcements are due to the nature of the natural fibres as well as the manufacturing process used in the production of the material. The fibre-reinforced-composite in question consists of a polymer matrix containing thin, randomly orientated, natural-fibre reinforcements. Needle-punching is used to entangle the fibres, which are then bonded into the matrix. This process results in a thin, flat composite which is used as the outer layers in a laminate, which sandwich a honeycomb filler. Figures 1.2(a) and 1.2(b) show the entangled fibres bonded into the matrix and the needle-punched fibres before bonding respectively. Figure 1.3 shows the final product laminating the honeycomb filler.

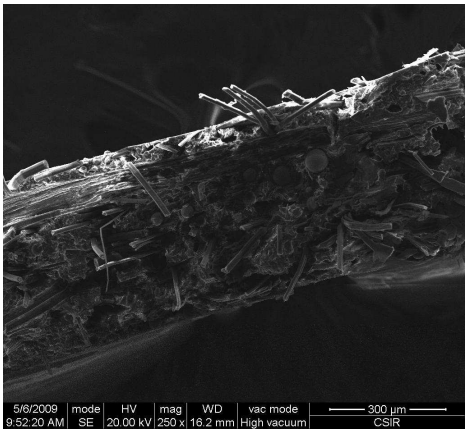

(a) Fibres bonded into matrix after needlepunching process

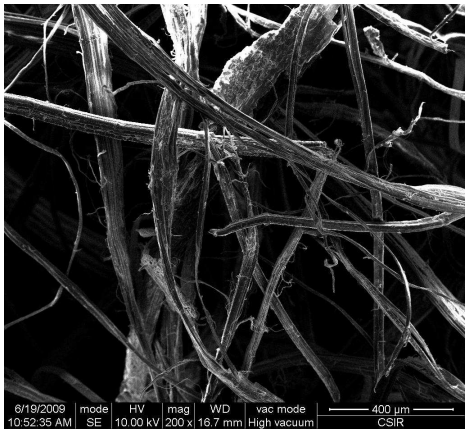

(b) Fibres entangled after needlepunching process

Fig. 1.2: The entangled fibres post needlepunching process

Fig. 1.3: The fibre-matrix composite bonded and used as the outer layers of a laminate. (image courtesy of the CSIR, Port Elizabeth)

By first analysing a simple model of the material and later adding more complicated features, the effects of small alterations to the material can be investigated, without significant additional trouble or cost. Thus via this bottom-up approach it is possible to understand exactly which characteristics of the microstructure have the most bear-

ing on the properties of the final material, for example the geometry of the fibres in the matrix or the material properties of the individual components. This ultimately means that an optimal design may be reached with only a small number of experimental tests needed to verify the results. Once the results from the model accurately mimic those reached experimentally, more complex loading conditions can be created and investigated computationally.

In this thesis a micro-macro modelling approach is taken in a linear elastic, small strain context using finite element modelling. The micro-macro model details the microstructure only at the length scale of the heterogeneity, and uses volume averages over the micro-domain as the macroscopic counterparts. Due to the fact that the length scale of the fibres is orders of magnitude smaller than the length scale of the working material specimen it is unrealistic to model the entire domain, thus the micro-macro technique is well suited to this application.

1.2 Objectives and limitations

The aim of this thesis is to develop and implement a methodology for determining the effective properties of random fibre-reinforced composites using the finite element method. An homogenisation technique is developed in which the "effective" properties of the material are determined, such that the heterogeneous material may be substituted with an effectively equivalent homogeneous and macroscopically isotropic material. The advantage of this substitution is a significant reduction in computational expense at the macroscopic level of the structure, as the heterogeneities need only be modelled at the microscopic level.

Due to the heterogeneities in the microstructure no assumptions can be made about the constitutive behaviour of the material at the macro-scale. Instead a detailed physical model of the microstructure is developed and linked to the macro-scale through

common variables. The constitutive relationship at the macro-scale is thus allowed to develop from the microscopic behaviour. A representative volume element (RVE) captures the response of the microstructure which is assumed to exist at every material point in the macroscopic domain. The macroscopic and microscopic domains are linked according to the assumption that the local macroscopic deformation and stress tensors are equal to those averaged over the RVE [9].

The main limitation to this endeavour is computational expense. Due to the complexity of the microstructure and the degree of scale separation between the working material specimen and the heterogeneity in the microstructure the problem is computationally laborious. Various assumptions make the model viable, such as the assumptions of small strains and linear elasticity, which allow the problem to be solved in a single iteration. It is also important to choose an RVE that is truly representative of the microstructure while also being computationally viable.

1.3 Approaches to micro-macro modelling

The micro-macro approach has been taken for a number of applications, involving various microstructures. It can be applied to any problem in which heterogeneities in the microstructure affect the material behaviour of the macro-domain.

One of the main limitations in the micro-macro modelling is the computational expense of attempting to create and analyse a detailed microstructure accurately. It is important to create as efficient a computational implementation as possible as is emphasised in the work of [21].

The applications of this modelling technique for materials with a heterogeneous microstructure are abundant and there is a growing literature database on the topic. While the general theory is common to all applications, various aspects of different microstructures can greatly affect the necessary route taken in the modelling of the material.

A particular concern in fibre-reinforced composites is the correct sizing of the RVE when the fibre dispersion within the matrix is random. The sizing of RVEs and the importance thereof has been addressed in [28], [19] and [13]. In cases where the microstructure is periodic as in [4], [6] and [7] (discussed below) a unit cell is quite often used to represent the entire microstructure.

The manner in which a problem is approached depends entirely on the nature of the application.

For example, Hofstetter et al [10] used the micro-macro approach in the modelling of wood. Due to the many tiers of heterogeneities at different length scales, a four-tiered multiscale analysis was executed, but the material parameters at each level were kept relatively simple.

The model was linear elastic and time-independent. The first stage of the homogenisation was that of a mixture of hemicellulose, lignin and water at a length scale of tens of nanometers. This mixture was modelled as spherical inclusions that build up a polymer network. At a length scale of approximately one micron the cell wall material was modelled as cylindrical inclusions of crystalline and amorphous cellulose embedded in a polymer matrix. The third step of the homogenisation involved the softwood material. This exists at approximately 100 microns and is comprised of lumen (cylindrical inclusions) embedded in the cell wall material that comprised the second homogenisation step. The fourth and final step of the homogenisation exists at a length scale of several millimetres where vessels (cylindrical inclusions) are embedded in the softwood material.

The predicted elastic moduli were compared to experimental results for hardwood and softwood. The correlation was generally good and the discrepancies may have been due to the fact that the orientation of various inclusions was not taken into account in detail.

Miehe et al [18] applied the method to pollycrystalline materials. The deformations were non-isothermal and inelastic, and at large strains. The microstructure is made

up of an assembly of single crystal grains and the work focusses on the response of the grains using both the thermomechanical and deformation boundary problems.

Multi-scale modeling lends itself to biomechanics, in particular, tissue systems have been modeled using this methodology.

Stylianopolous et al [26] and Maceri et al [16] used the micro-macro modelling technique to model the collagen networks in human tissue systems. These networks exist in blood vessel walls, skin, valves and tendons in both native and engineered tissue systems. Understanding these systems is important in the event of surgical intervention and in the design of prosthetics for the human body.

Maceri et al looked at soft collageneous tissues with regular fibre arrangements (RSCTs). Both uni- and multidirectional fibre arrangements were investigated, where a multidirectional situation consists of layers of unidirectional fibre arrangements. The fibres were modeled as being isotropic and non-linear elastic. Two homogenisation steps were used; first the crimped fibres were homogenised to an equivalent straight fibre, thus a unidirectional RSCT became a straight-fibre-reinforced composite material. Then an homogenisation was performed on the heterogeneous macro tissue containing the homogenised crimped fibres.

The approach taken by Stylianopolous et al was quite different to that of Maceri et al as the interaction of the long, thin, interconnected collagen fibres was stressed and thus the geometrical structure as well as the material properties added the most complexity to the model. The collagen networks were analysed at a length scale of a few micrometres, while the tissue on the macroscale was analysed at about one centimetre.

Emphasis was on the random arrangement of the collagen fibres and the interaction between them. A three-dimensional model was developed so as to fully allow

the fibres to re-align themselves as the tissue deformed. The fibres' interactions are complex, involving entanglements, rigid cross-links and bifurcations and the detailed geometrical model was important as the interaction between the fibres accommodates the majority of the strain in the systems.

A Galerkin finite element model was used to analyse the macroscopic domain while the micro problem was solved via a force balance on the system. Due to the non-linearity of the problem the model was fully iterative. When compared to in vitro mechanical test data the Poisson's ratio calculated was comparable to that found experimentally. The model allowed an understanding of the effects of the heterogeneity in the networks on the living tissue.

Microstructures involving fibre reinforcements have been investigated in [7], [6], [4], [24] and [20].

In [6] and [7] Feyel and Chaboche investigate a fibre reinforced composite for use in the aeronautical industry. New innovations are currently being analysed in this industry as materials that are both light and strong, and with high melting points can be used to lighten the components and thereby increase the thrust in turbo machines. The fibre reinforcements are periodic and, as such, the RVE analysed consisted of a unit cell. The finite element method was used to investigate, in particular, the interaction of the fibre with the matrix. In these sorts of materials it is emphasised that the interface between the two components is paramount to the performance of the material, thus debonding in the material is emphasised in the work.

Belsky et al [4] developed a multiscale model of laminated composite shell structures. The unit cell was used again, but it was noted that this assumption of periodicity does not hold in regions of high stress concentration. Sansalone [24] also analysed a fibre matrix composite, and focussed on a method that showed how the length scale and the arrangement of the microstructure affects the elastic response of the material. In this way, an optimum arrangement of fibre reinforcements may be found.

Pan et al [20] dealt with random chopped fibre composites (RaFCs) in which the fibre reinforcements are short (in this case, half the length of the RVE), and thus an RVE will have fibres originating and terminating within its boundaries. The focus was on high volume fractions, so the algorithm used to create the microstructure allowed the fibres to curve around each other in order to allow a large number of fibres to exist in the material. As the model was linear elastic it was only analysed at the micro-level.

The micro-macro method has also been used by Wriggers et al [30], in the modelling of hard cement paste (HCP) with regard to investigating frost damage in the material. Here the emphasis was on the expansion of water molecules in the HCP on freezing and thus the relationship between temperature, water content and expansion and damage was investigated.

The microstructure of HCP was modelled at a length scale of a few hundreds of microns with varying water content. The macrodomain operated at a length scale of tens of millimetres. The microdomain was modelled as small, irregular inclusions in a matrix.

1.4 Outline of thesis

The rest of this thesis is structured as follows: Chapter 2 provides the theory used in the thesis. An overview of classical continuum mechanics within a small strain, linear elastic context is presented. Homogenisation theory is then discussed in general in terms of volume averaging and the resulting necessary boundary conditions. As the thesis serves as an initial step in the development of a fully nonlinear, iterative micro-macro model it is important to recognise that the enforcement of the boundary conditions on the micro-domain can become non-trivial in such a model. As such, two methods of enforcing these constraints are discussed. The extraction of the elastic material properties is then explained followed by the derivation of the Reuss and

Voigt bounds, which are used in bounding the computational results. A tightening of these bounds through partitioning of the domain is then discussed.

Chapter 3 starts with an overview of the finite element method, once again for small strain, linear elasticity. The finite element implementations of the methods (presented in Chapter 2) of enforcing the boundary conditions are explained along with the extraction of elastic modulus information. The results of the investigations into these methods are then presented and discussed.

The methodology used for this thesis, which closely follows that of Zohdi and Wriggers [31] follows in Chapter 4. This includes the method of sizing the RVE and a discussion of expectations on the results. The implementation of the model within the various software utilised is also included here as well as the modelling approximations used in the process.

Results of the investigation are shown and discussed in Chapter 5. Finally conclusions are drawn and recommendations for future work are given in Chapter 6.

2

Micro-macro modelling

In this chapter the general theoretical background to the thesis is set out. Classical continuum mechanics, with emphasis on linear elastic and small strain theory, is presented and the weak form of the general problem is derived. Section 2.1 follows the theory set out by [22] and [15]. The general method for an homogenisation process is presented. For an iterative problem boundary condition enforcement at the microscale becomes important and two methods by which these can be implemented are set out. The specific method by which the effective elastic material properties are calculated in this thesis is then explained and the expected bounds on the results are discussed.

2.1 Overview of classical continuum mechanics

In modelling a material as a continuum it is assumed that a macroscopic, three dimensional body, initially occupying the domain, Ω at time, $t = 0$, completely fills this domain and is continually distributed across it. As shown in Figure 2.1, a material point inside the reference domain is described by the position vector, $\boldsymbol{x}$ and all properties of the material are then functions of $\boldsymbol{x}$ and t. The motion of the body is orientation preserving, so every element of non-zero volume in Ω is mapped to an element of non-zero volume in Ω_t, which is the current domain. Thus the determinant of the Jacobian, $J = \det(\partial \boldsymbol{y}_i / \partial \boldsymbol{x}_j)$, is positive.

2.1.1 Infinitesimal strain

For the displacement vector $\boldsymbol{u}(\boldsymbol{x}, t)$, the strain tensor is defined as,

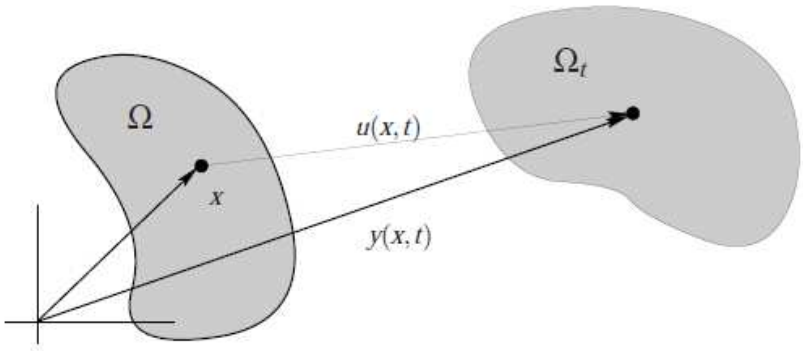

Fig. 2.1: Current and undeformed configurations of an arbitrary material body (image courtesy of [22])

$$\boldsymbol{\eta}(\boldsymbol{u}) = \frac{1}{2}[\nabla \boldsymbol{u} + (\nabla \boldsymbol{u})^T + (\nabla \boldsymbol{u})^T \nabla \boldsymbol{u}]\,. \tag{2.1}$$

$\boldsymbol{\eta}$ measures the deformation of a body, so for a rigid body motion $\boldsymbol{\eta} = 0$. The diagonal components of strain, η_{ij} for $i = j$ are the direct strains, and measure the change in length of a fibre originally aligned with the axis x_i. The off-diagonal components of strain, η_{ij} for $i \neq j$ measure the change in angle between two fibres, originally perpendicular to each other and lying parallel to the x_i and x_j axes.

If the displacement gradient $(\nabla \boldsymbol{u})$ is small enough that the non-linear terms become negligible, the body is said to undergo infinitesimal strain, which is defined as

$$\boldsymbol{\varepsilon} = \frac{1}{2}[\nabla \boldsymbol{u} + (\nabla \boldsymbol{u})^T]\,. \tag{2.2}$$

Defining the change in volume per unit volume,

$$\frac{\Delta V}{V} = \mathrm{div}\boldsymbol{u}\,. \tag{2.3}$$

So for an incompressible material, that is, one in which no change in volume occurs,

$$\mathrm{div}\boldsymbol{u} = \mathbf{0}\,. \tag{2.4}$$

2.1.2 Stress and the balance of linear and angular momentum

A body can be subjected to two types of force, body forces and surface tractions. A body force, $\mathbf{b}$, examples of which are the gravitational force and magnetic forces, is exerted by an external means on the body and is the force per unit volume exerted on the material point $\boldsymbol{x}$ at time t. Surface tractions, denoted as $\mathbf{t}$, act on a surface or part of the domain boundary with unit normal $\boldsymbol{n}$ and are measured in the force per unit area. Cauchy's Theorem states that there exists a second-order tensor, $\boldsymbol{\sigma}$, such that

$$\boldsymbol{\sigma n} = \boldsymbol{t} \tag{2.5}$$

where $\boldsymbol{\sigma}$ is called the Cauchy stress.

If Ω_t' is an arbitrary part of Ω_t, the total force acting thereon is equal to the rate of change of linear momentum of Ω_t', this, the balance of linear momentum, is expressed in terms of integrals over the reference domain, Ω',

$$\int_{\Omega'} \rho\ddot{\boldsymbol{u}}\mathrm{d}x = \int_{\Omega'} \mathbf{b}\mathrm{d}x + \int_{\Gamma'} \boldsymbol{t}\mathrm{d}s \tag{2.6}$$

where ρ is the mass density of the body. Thus the Cauchy stress satisfies the equation of motion,

$$\mathrm{div}\boldsymbol{\sigma} + \mathbf{b} = \rho\ddot{\boldsymbol{u}}\,. \tag{2.7}$$

If the problem is time-independent, that is, acceleration is equal to zero, then Equation (2.7) becomes the Equilibrium equation,

$$\mathrm{div}\boldsymbol{\sigma} + \mathbf{b} = \mathbf{0}\,. \tag{2.8}$$

The total moment acting on Ω_t' is equal to the rate of change of angular momentum of Ω_t', this, the balance of angular momentum, is expressed in terms of integrals over the reference domain, Ω_t',

$$\int_{\Omega'} \mathbf{x} \times \rho\ddot{\boldsymbol{u}}\ \mathrm{d}x = \int_{\Omega'} \mathbf{x} \times \mathbf{b}\ \mathrm{d}x + \int_{\Gamma'} \mathbf{x} \times \boldsymbol{t}\ \mathrm{d}s\,. \tag{2.9}$$

From this we can deduce that the Cauchy stress is symmetric,

$$\boldsymbol{\sigma}^T = \boldsymbol{\sigma}\,. \tag{2.10}$$

Thus the governing equations resulting from the balance of linear and angular momentum are

$$\mathrm{div}\boldsymbol{\sigma} + \mathbf{b} = \rho\ddot{\boldsymbol{u}}, \tag{2.11}$$

$$\boldsymbol{\sigma}^T = \boldsymbol{\sigma}\,. \tag{2.12}$$

As we are working in the infinitesimal strain context all of the above equations can be solved on the reference domain.

2.1.3 Boundary conditions

The governing equations must be accompanied by a set of boundary conditions, to be specified over the entire domain boundary, Γ. These boundary conditions can be one of two types. The first are Dirichlet, or essential, boundary conditions where the displacement of the boundary is prescribed on Γ_u. At least a part of the domain boundary must be a Dirichlet boundary, that is, for the body to be in equilibrium

there must be at least one fixed part of the boundary. The second type of boundary conditions are Neumann, or natural, boundary conditions. Here a surface traction is specified on a part of the domain boundary Γ_t. It is not required that any part of the boundary is a Neumann boundary. Dirichlet and Neumann boundaries are stated, respectively, as,

$$\boldsymbol{u} = c \qquad \text{on} \qquad \Gamma_u \quad \text{and} \tag{2.13}$$

$$\boldsymbol{t} = \boldsymbol{\sigma n} = \overline{\boldsymbol{t}} \qquad \text{on} \qquad \Gamma_t \,. \tag{2.14}$$

2.1.4 Linear elasticity

A linear elastic material is one in which the stress is linearly dependent on the infinitesimal strain,

$$\boldsymbol{\sigma} = \mathbb{E}\boldsymbol{\varepsilon} \tag{2.15}$$

or, in component form:

$$\sigma_{ij} = \mathbb{E}_{ijkl}\boldsymbol{\varepsilon}_{kl} \tag{2.16}$$

where $\mathbb{E}$ is the elasticity tensor and the above equations give the constitutive relationship of the material. In an homogeneous material ρ and $\mathbb{E}$ are independent of position.

A material in which there is no preferred direction is called an isotropic material and its response to a force is completely independent of its orientation. In the case of isotropy the constitutive equation can be expressed in terms of only two material constants, such as the Lamé moduli, λ and μ,

$$\boldsymbol{\sigma} = \lambda(\mathrm{tr}\boldsymbol{\varepsilon})\mathbf{I} + 2\mu\boldsymbol{\varepsilon} \,. \tag{2.17}$$

Any second order tensor $\boldsymbol{\tau}$ may be written as the sum of the deviatoric and spherical parts, $\boldsymbol{\tau}^{'}$ and $\boldsymbol{\tau}^{S}$, respectively,

$$\boldsymbol{\tau} = \boldsymbol{\tau}^{'} + \boldsymbol{\tau}^{S} \qquad \text{where:} \tag{2.18}$$

$$\boldsymbol{\tau}^{'} = \boldsymbol{\tau} - \frac{1}{3}(\mathrm{tr}\boldsymbol{\tau})\mathbf{I} \qquad \text{and} \qquad \boldsymbol{\tau}^{S} = \frac{1}{3}(\mathrm{tr}\boldsymbol{\tau})\mathbf{I}\,. \tag{2.19}$$

The uncoupled form of the constitutive relationship is then,

$$\boldsymbol{\sigma}^{'} = 2\mu\boldsymbol{\varepsilon}^{'} \tag{2.20}$$

$$\boldsymbol{\sigma}^{S} = \frac{1}{3}(\mathrm{tr}\boldsymbol{\sigma})\boldsymbol{I} = \frac{1}{3}(3\lambda + 2\mu)\mathrm{tr}\boldsymbol{\varepsilon}\boldsymbol{I} = 3(\lambda + \frac{2}{3}\mu)\boldsymbol{\varepsilon}^{S} = 3\kappa\boldsymbol{\varepsilon}^{S} \tag{2.21}$$

where μ is the shear modulus and $\kappa = \lambda + \frac{2}{3}\mu$ is the bulk modulus. The forms that are used in this thesis are derived as follows. Firstly for the shear modulus we square both sides of equation (2.20), to get

$$\boldsymbol{\sigma}^{'} : \boldsymbol{\sigma}^{'} = (2\mu)^2\boldsymbol{\varepsilon}^{'} : \boldsymbol{\varepsilon}^{'} \tag{2.22}$$

then

$$2\mu = \sqrt{\frac{\boldsymbol{\sigma}^{'} : \boldsymbol{\sigma}^{'}}{\boldsymbol{\varepsilon}^{'} : \boldsymbol{\varepsilon}^{'}}} \tag{2.23}$$

and finally for the bulk modulus, from equation (2.21) we have

$$\mathrm{tr}\boldsymbol{\sigma} = 3\kappa(\mathrm{tr}\boldsymbol{\varepsilon}) \tag{2.24}$$

which is then written as

$$3\kappa = \frac{\mathrm{tr}\boldsymbol{\sigma}}{\mathrm{tr}\boldsymbol{\varepsilon}}\,. \tag{2.25}$$

The constitutive relationship can also be written in terms of the Young's modulus and Poisson's ratio. For a uniaxial test (shown in Figure 2.2) an isotropic rod is aligned

with the x_1 axis and subjected to a uniform stress field $\boldsymbol{\sigma}_{11} \neq 0$ (all other components of stress are zero). Due to the isotropy the specimen only experiences direct strains. Then,

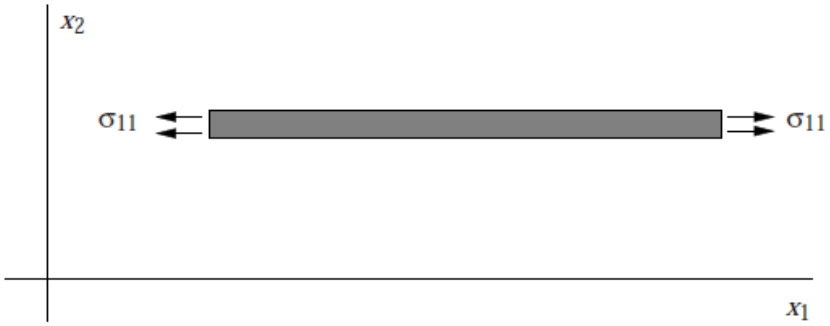

Fig. 2.2: A specimen in a state of uniaxial stress

$$E = \frac{\sigma_{11}}{\varepsilon_{11}} \qquad \text{(Young's modulus)} \quad ; \quad \nu = -\frac{\varepsilon_{22}}{\varepsilon_{11}} \qquad \text{(Poisson's ratio)}\,. \tag{2.26}$$

Using these material coefficients the constitutive relation becomes,

$$\boldsymbol{\varepsilon} = E^{-1}[(1+\nu)\boldsymbol{\sigma} - \nu(\mathrm{tr}\boldsymbol{\sigma})\mathbf{I}]\,. \tag{2.27}$$

The bulk and shear moduli can also be defined according to physical tests. Consider a cubic specimen under hydrostatic pressure as shown in Figure 2.3. Note here that $\sigma_{11} = \sigma_{22} = \sigma_{33} = \boldsymbol{\sigma}$ The bulk modulus is then the resistance of the speciment to a change in volume when compressed.

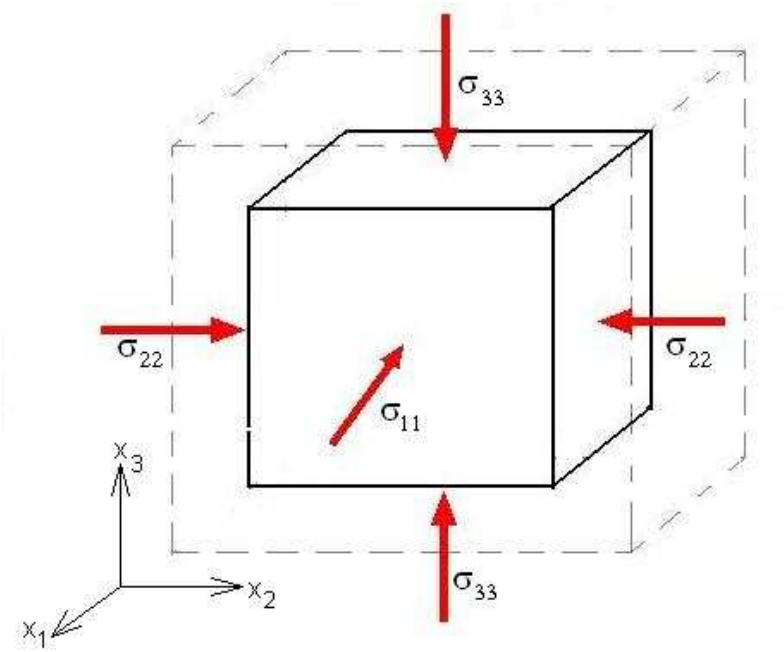

Fig. 2.3: A specimen under hydrostatic pressure

The ratio of shear stress to shear strain is given by the shear modulus. If a specimen is sheared, as shown in Figure 2.4, then the shear modulus can be written as,

$$\mu = \frac{\sigma_{12}}{2\varepsilon_{12}} \tag{2.28}$$

The bulk and shear moduli can then be expressed in terms of the Young's modulus and Poisson's ratio,

$$\kappa = \frac{E}{3(1-2\nu)} \quad ; \quad \mu = \frac{E}{2(1+\nu)}\,. \tag{2.29}$$

In this thesis we deal chiefly with the bulk and shear moduli in the form shown in equations (2.23) and (2.25).

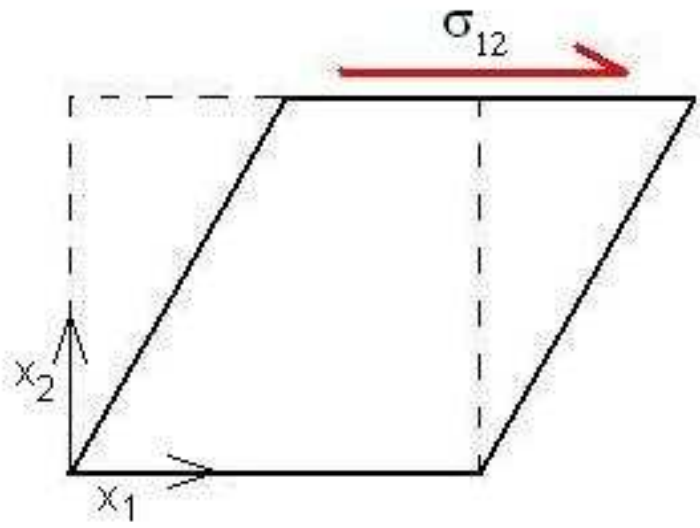

Fig. 2.4: A specimen in shear

2.1.5 The weak formulation

The finite element method uses the weak form of the governing equation and the Galerkin method. The weak form is developed as follows.

The weak form is derived from the preceding strong form (Equations (2.8), (2.13) (2.14) and (2.15)) using an arbitrary displacement field $\boldsymbol{w}$, which satisfies the homogeneous Dirichlet boundary condition: $\boldsymbol{w} = \mathbf{0}$ on Γ_u. Taking the scalar product of $\boldsymbol{w}$ and the Equilibrium equation (2.8) and integrating gives,

$$\int_{\Omega} \mathrm{div}\boldsymbol{\sigma} \cdot \boldsymbol{w} \, \mathrm{dV} = \int_{\Omega} \boldsymbol{b} \cdot \boldsymbol{w} \, \mathrm{dV} \,. \tag{2.30}$$

Applying the divergence theorem to the left hand side of (2.30), we get,

$$\int_{\Omega} \mathrm{div}\boldsymbol{\sigma} \cdot \boldsymbol{w} \, \mathrm{dV} = \int_{\Gamma} \boldsymbol{\sigma}\boldsymbol{n} \cdot \boldsymbol{w} \, \mathrm{dA} - \int_{\Omega} \boldsymbol{\sigma} \colon \nabla \boldsymbol{w} \, \mathrm{dV} \,. \tag{2.31}$$

As $\boldsymbol{w} = \mathbf{0}$ on Γ_u and $\boldsymbol{\sigma}\boldsymbol{n} = \overline{\boldsymbol{t}}$ on Γ_t, Equation (2.30) becomes,

$$\int_{\Omega} \mathrm{div}\boldsymbol{\sigma} \cdot \boldsymbol{w} \ \mathrm{dV} = \int_{\Gamma_{\boldsymbol{t}}} \overline{t} \cdot \boldsymbol{w} \ \mathrm{dA} - \int_{\Omega} \boldsymbol{\sigma} \colon \nabla \boldsymbol{w} \ \mathrm{dV} \,. \tag{2.32}$$

From the fact that stress is symmetric, $\boldsymbol{\sigma} \colon \nabla \boldsymbol{w} = \boldsymbol{\sigma} \colon \frac{1}{2}(\nabla \boldsymbol{u} + (\nabla \boldsymbol{u})^T) = \boldsymbol{\sigma} \colon \boldsymbol{\varepsilon}(\boldsymbol{w})$, we can express the weak form of the boundary value problem as,
for any arbitrary function $\boldsymbol{w}$, find the displacement $\boldsymbol{u}$ such that,

$$\int_{\Omega} \boldsymbol{\sigma} \colon \boldsymbol{\varepsilon}(\boldsymbol{w}) \mathrm{dV} = \int_{\Omega} \boldsymbol{b} \cdot \boldsymbol{w} \mathrm{dV} + \int_{\Gamma_t} \overline{\boldsymbol{t}} \cdot \boldsymbol{w} \mathrm{dA} \qquad \text{s.t.} \quad \boldsymbol{u} = \overline{c} \quad \text{on} \quad \Gamma_u \,. \tag{2.33}$$

2.1.6 Voigt notation

It is convenient to use Voigt notation when implementing the finite element method, which is the method used in this thesis. To do this we express the stress and strain tensors, $\boldsymbol{\sigma}$ and $\boldsymbol{\varepsilon}$ as column vectors,

$$\boldsymbol{\sigma} = [\sigma_{11} \quad \sigma_{22} \quad \sigma_{33} \quad \sigma_{12} \quad \sigma_{13} \quad \sigma_{23}]^T \tag{2.34}$$

$$\varepsilon = [\varepsilon_{11} \quad \varepsilon_{22} \quad \varepsilon_{33} \quad 2\varepsilon_{12} \quad 2\varepsilon_{13} \quad 2\varepsilon_{23}]^T \tag{2.35}$$

thus $\boldsymbol{\sigma} \colon \boldsymbol{\varepsilon} = \sigma_{ij}\varepsilon_{ij}$ can be written, using the Voigt notation above, as $\boldsymbol{\sigma}^T\boldsymbol{\varepsilon}$ or $\boldsymbol{\varepsilon}^T\boldsymbol{\sigma}$.

Also, the expression,

$$[\mathrm{div}\boldsymbol{\sigma}] = \begin{bmatrix} \frac{\partial \sigma_{11}}{\partial x_1} + \frac{\partial \sigma_{12}}{\partial x_2} + \frac{\partial \sigma_{13}}{\partial x_3} \\ \frac{\partial \sigma_{21}}{\partial x_1} + \frac{\partial \sigma_{22}}{\partial x_2} + \frac{\partial \sigma_{23}}{\partial x_3} \\ \frac{\partial \sigma_{31}}{\partial x_1} + \frac{\partial \sigma_{32}}{\partial x_2} + \frac{\partial \sigma_{33}}{\partial x_3} \end{bmatrix} \tag{2.36}$$

simply becomes $\mathrm{div}\boldsymbol{\sigma} = \nabla_S \boldsymbol{\sigma}$ when using Voigt notation, where the appropriate matrix of partial derivatives ∇_S is defined as,

$$\nabla_S = \begin{bmatrix} \frac{\partial}{\partial x_1} & 0 & 0 & \frac{\partial}{\partial x_2} & \frac{\partial}{\partial x_3} & 0 \\ 0 & \frac{\partial}{\partial x_2} & 0 & \frac{\partial}{\partial x_1} & 0 & \frac{\partial}{\partial x_3} \\ 0 & 0 & \frac{\partial}{\partial x_3} & 0 & \frac{\partial}{\partial x_1} & \frac{\partial}{\partial x_2} \end{bmatrix} \,. \tag{2.37}$$

Thus the strain, as defined in Equation (2.2), can be written in terms of the displacements,

$$\boldsymbol{\varepsilon}(\boldsymbol{u}) = \nabla_S^T \boldsymbol{u} \tag{2.38}$$

and the equilibrium and constitutive equations become,

$$\nabla_S \boldsymbol{\sigma} + \boldsymbol{b} = \mathbf{0} \tag{2.39}$$

$$\boldsymbol{\sigma} = \mathbf{D}\boldsymbol{\varepsilon} = \mathbf{D}\nabla_S \boldsymbol{u} \tag{2.40}$$

respectively, where $\mathbf{D}$ is the elasticity matrix,

$$\mathbf{D} = \frac{E}{(1+\nu)(1-2\nu)} \begin{bmatrix} 1-\nu & \nu & \nu & 0 & 0 & 0 \\ \nu & 1-\nu & \nu & 0 & 0 & 0 \\ \nu & \nu & 1-\nu & 0 & 0 & 0 \\ 0 & 0 & 0 & \frac{1}{2}(1-2\nu) & 0 & 0 \\ 0 & 0 & 0 & 0 & \frac{1}{2}(1-2\nu) & 0 \\ 0 & 0 & 0 & 0 & 0 & \frac{1}{2}(1-2\nu) \end{bmatrix}. \tag{2.41}$$

So Equation (2.33), the weak form, in matrix form using Voigt notation, is written as,

$$\int_\Omega (\nabla_S^T \boldsymbol{w})^T \mathbf{D} \nabla_S \boldsymbol{u} \, \mathrm{dV} = \int_\Omega \boldsymbol{w}^T \boldsymbol{b} \, \mathrm{dV} + \int_{\Gamma_t} \boldsymbol{w}^T \overline{\boldsymbol{t}} \, \mathrm{dA} \,. \tag{2.42}$$

2.2 Homogenisation theory

Let a sample of the material occupy a domain $\Omega \in \mathbb{R}^3$. The body is in equilibrium with surface tractions $\mathbf{t}$ and body forces $\mathbf{f}$. The boundary of the domain, $\overline{\partial\Omega} = \overline{\Gamma_u \cup \Gamma_t}$ is made up of displacement boundaries, Γ_u, and traction boundaries, Γ_t, all of which are prescribed. The domain is shown in Figure 2.5. The elasticity tensor $\mathbb{E}$ varies across the domain due to the heterogeneities within the material. The variational boundary value problem for the macro-domain is given in Equation (2.33).

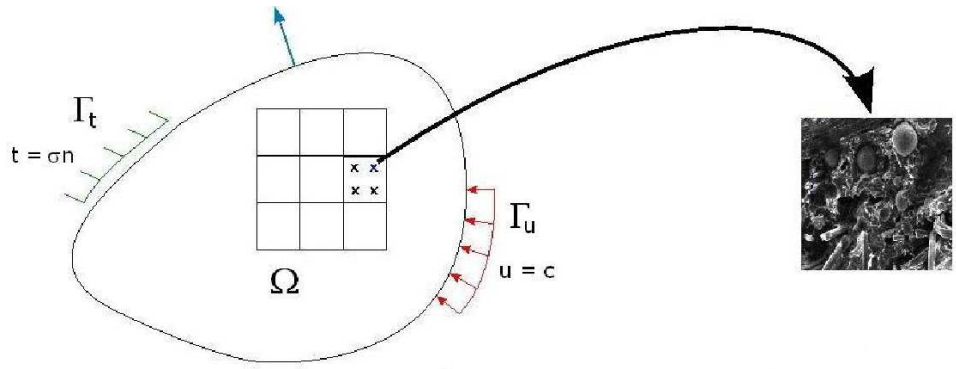

Fig. 2.5: The macro-scopic domain with magnified heterogeneous structure of microdomain

A representative volume element (RVE) is assumed to exist at every material point of the macroscopic domain. This RVE is discretised and relevant boundary conditions are applied.

The analysis on the RVE will give an effective macroscopic linear elasticity tensor, $\mathbb{E}^*$, which relates the averages of the microscopic stress, $\boldsymbol{\sigma}$, and the microscopic strain, $\boldsymbol{\varepsilon}$,

$$\langle \boldsymbol{\sigma} \rangle_{\Omega} = \mathbb{E}^* : \langle \boldsymbol{\varepsilon} \rangle_{\Omega} \,. \tag{2.43}$$

In order to link the macro- and micro-problems, the boundary conditions on the RVE must ensure that the macroscopic stress power is equal to the average microscopic stress power, that is, they must satisfy Hill's condition [8],

$$\underbrace{\langle \boldsymbol{\sigma} : \dot{\boldsymbol{\varepsilon}} \rangle_{\Omega}}_{\text{averaged microscopic stress power}} = \underbrace{\langle \boldsymbol{\sigma} \rangle_{\Omega} : \langle \dot{\boldsymbol{\varepsilon}} \rangle_{\Omega}}_{\text{macroscopic stress power}} \tag{2.44}$$

where the averaged quantities are defined as follows,

$$\langle \cdot \rangle := \frac{1}{|\Omega|} \int_{\Omega} (\cdot) \, \mathrm{d}\Omega \,. \tag{2.45}$$

This condition is satisfied by three types of boundary conditions, linear displacement, constant traction and periodic displacements and anti-periodic tractions, which are shown in equations (2.46) through (2.49), where $\mathcal{E}$ and $\mathcal{T}$ are the macroscopic strain and stress respectively. The physical meaning of these boundary constraints is illustrated in Figures 2.6(a), 2.6(b) and 2.6(c).

$$\mathbf{u}|_{\partial\Omega} = \mathcal{E}\mathbf{x} \qquad \text{(linear displacement)} \tag{2.46}$$

$$\mathbf{t}|_{\partial\Omega} = \mathcal{T}\mathbf{n} \qquad \text{(constant traction)} \tag{2.47}$$

$$\mathbf{u}^+ - \mathbf{u}^-|_{\partial}\Omega = \mathcal{E}(\mathbf{x}^+ - \mathbf{x}^-) \qquad \text{(periodic displacement)} \tag{2.48}$$

$$\mathbf{t}\mathbf{x}^+ + \mathbf{t}\mathbf{x}^- = \mathbf{0} \qquad \text{(anti-periodic traction)}\,. \tag{2.49}$$

The problem stated in the preceding section applies to a linear problem in a small

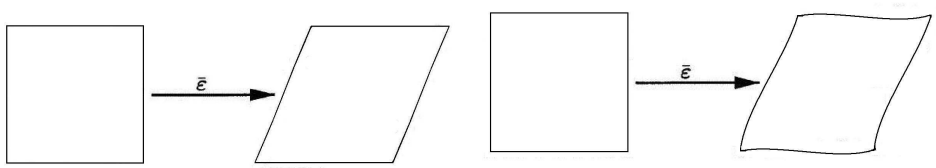

(a) Linear displacement boundary constraint

(b) Constant traction boundary constraint

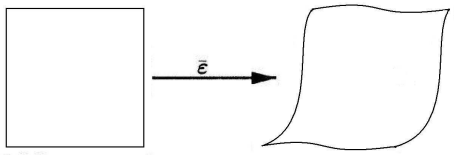

(c) Periodic displacements and anti-periodic traction boundary constraint

Fig. 2.6: The boundary conditions on the micro-domain which satisfy Hill's condition

strain context. The method can be expanded to be effective for a fully iterative, non-linear problem where an homogeneous macro-domain would be defined and a relevant strain field applied. At each integration point an RVE would be defined and

discretised. Strain field information would be passed to the RVE from the macro-domain and the boundary value problem on the micro-domain solved. Stress field information and an updated effective tangent modulus would be returned to the macro-domain. The problem would be solved via an iterative process.

2.3 Boundary condition enforcement on the RVE

While the general aim in volume averaging problems is to glean constitutive parameters using a detailed model of the microstructure, there are a number of ways to go about this. In particular, management of the boundary constraints is discussed here, as this becomes non-trivial when the problem is iterative due to non-linearity.

During the course of this thesis various algorithms were tested for simple problems, including an homogenous specimen, in order to fully understand the different implementation options available. It has been argued that while linear displacement and constant traction boundary conditions give upper and lower bounds, respectively, on the constitutive tensor a periodic displacement/anti-periodic traction boundary constraint will give the most accurate result regardless of whether the microstructure in question is, in fact, periodic or random [14], [25]. In this thesis it was chosen to implement a final model incorporating only the linear displacement boundary condition, understanding that it would provide only an upper bound to the problem. During the initial stages of the investigation, however, the periodic boundary constraint was implemented in a basic problem as an aid to understanding the various boundary constraint options.

2.3.1 Lagrange multipliers

Lagrange multipliers have been used in the enforcement of the various boundary constraints by Miehe [17], Kousnetsova [14], and Smit [25]. This method entails the use of an extra unknown which acts as a “force” to constrain the boundaries as prescribed.

In investigating the lagrange multiplier method of enforcing boundary constraints only the algorithm for the periodic problem was executed on the micro-domain. The method as presented by Miehe was tested and gave satisfactory results according to an homogeneous R.V.E. with a known elastic modulus.

The enforcement of the periodic boundary constraint is as follows. The periodic boundary constraint involves the definition of positive and negative boundaries, such that each positive boundary has a corresponding negative boundary situated on the opposite side of the domain as shown in Figure 2.7. The condition of periodic dis-

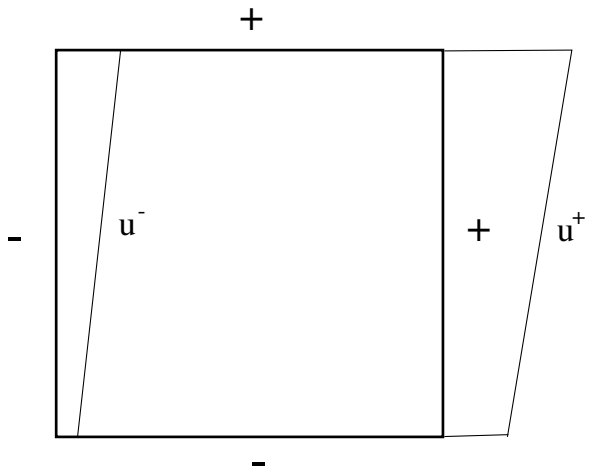

Fig. 2.7: RVE with positive (+) boundaries and corresponding negative (-) boundaries

placements and anti-periodic tractions can then be stated as,

$$[(\mathbf{u}^+ - \mathbf{u}^-) - \mathcal{E}(\mathbf{x}^+ - \mathbf{x}^-)]\pi = \mathbf{0}, \qquad \mathbf{t}^+ + \mathbf{t}^- = \mathbf{0} \tag{2.50}$$

where the superscripts + and − denote quantities on the positive or negative boundaries as defined in Figure 2.7. The system of equations to be solved now contains an added variable π which is the lagrange multiplier and enforces the boundary con-

straint. The finite element method is used to solve the system and the implementation is presented in Chapter 3.

2.3.2 Penalty method

Wriggers et al [27] used the penalty method to enforce the boundary conditions. This method was also investigated, but only for the linear displacement boundary constraint. While this boundary condition is simple to apply directly, the method was nonetheless implemented with a view to fully understanding the process in the interest of future work where both the linear displacement and constant traction boundary conditions would be implemented for a fully iterative problem. Thus consistency in the application of the boundary conditions would be desirable.

The advantage of using the penalty method is that the prescribed displacements are imposed approximately through the penalty term, thus the global stiffness matrix can be assembled and used without the need to eliminate nodes at which the displacements are known.

The method was used within a finite strain context, where the equivalent quantities to stress and strain (in the small strain problem) are the 1st Piola-Kirchhoff stress tensor, $\boldsymbol{P}$ and the deformation gradient, $\boldsymbol{F}$. For this thesis only the small strain problem is relevant, thus the problem will be presented accordingly.

The linear displacement boundary constraint, shown in equation (2.46) is reproduced here for convenience,

$$\mathbf{u}|_{\partial\Omega} = \mathcal{E}\mathbf{x} \qquad \text{where} \qquad \mathcal{E} = \langle \boldsymbol{\varepsilon} \rangle \,.$$

This is enforced through the use of a penalty term, which is added to the standard weak form. For the linear displacement boundary condition, the penalty term takes the form,

$$\alpha_{LD} \int_{\partial V} |\boldsymbol{u} - \mathcal{E}\boldsymbol{x}|^2 dA \tag{2.51}$$

where α_{LD} is the linear displacement penalty parameter. The finite element analysis used to solve this problem is presented in Chapter 3.

2.4 Determining the elastic modulus

In the case of a macroscopically anisotropic material one would need to perform six linear independent loadings of either the form, $\mathbf{u}|_{\partial\Omega} = \mathcal{E}^{(I-VI)}.\,\mathbf{x}$, or $\mathbf{t}|_{\partial\Omega} = \mathcal{T}^{(I-VI)}.\,\mathbf{n}$ (which are the linear displacement and constant traction loadings respectively) in order to determine the effective macroscopic linear elasticity tensor $\mathbb{E}^*$. However, the random nature of the microstructure leads to an assumption that the material is effectively isotopic at the macro-scale. Due to this assumption of macroscopic isotropy the stresses and strains obtained from one loading case are sufficient. The effective elastic modulus can be expressed using two independent constants, the bulk and shear moduli, as discussed in Section (2.1.4), and defined using the averaged stresses and strains as in the form of equations (2.23) and (2.25),

$$3\kappa^* :\, = \frac{\langle \frac{1}{3}\mathrm{tr}\boldsymbol{\sigma}\rangle_\Omega}{\langle \frac{1}{3}\mathrm{tr}\boldsymbol{\varepsilon}\rangle_\Omega} \qquad \text{and} \qquad 2\mu^* :\, = \sqrt{\frac{\langle \boldsymbol{\sigma}'\rangle_\Omega :\, \langle \boldsymbol{\sigma}'\rangle_\Omega}{\langle \boldsymbol{\varepsilon}'\rangle_\Omega :\, \langle \boldsymbol{\varepsilon}'\rangle_\Omega}} \tag{2.52}$$

In this thesis, only the linear displacement boundary condition is implemented for an analysis of the fibre-reinforced composite. It satisfies Hill's condition as follows.

From equation (2.44), Hill's condition states that,

$$\underbrace{\langle \boldsymbol{\sigma} :\, \dot{\boldsymbol{\varepsilon}}\rangle_\Omega}_{\text{averaged microscopic stress power}} \quad = \quad \underbrace{\langle \boldsymbol{\sigma}\rangle_\Omega :\, \langle \dot{\boldsymbol{\varepsilon}}\rangle_\Omega}_{\text{macroscopic stress power}}$$

Focussing on the right hand side,

$$\mathrm{RHS} = \left(\frac{1}{|\Omega|}\int_\Omega \boldsymbol{\sigma}\,\mathrm{d}\Omega\right) :\, \left(\frac{1}{|\Omega|}\int_\Omega \boldsymbol{\varepsilon}\,\mathrm{d}\Omega\right)$$

using the definition of small strain we get,

$$= \left(\frac{1}{|\Omega|}\int_\Omega \boldsymbol{\sigma}\,\mathrm{d}\Omega\right) : \left(\frac{1}{|\Omega|}\int_\Omega \frac{1}{2}(\nabla\boldsymbol{u} + (\nabla\boldsymbol{u})^T)\,\mathrm{d}\Omega\right)$$

integrating by parts and noticing that non-boundary terms disappear,

$$= \left(\frac{1}{|\Omega|}\int_\Omega \boldsymbol{\sigma}\,\mathrm{d}\Omega\right) : \left(\frac{1}{2|\Omega|}\int_{\partial\Omega} (\boldsymbol{u}\otimes\boldsymbol{n} + \boldsymbol{n}\otimes\boldsymbol{u})\,\mathrm{d}\Omega\right).$$

Now re-writing the right hand side in index notation,

$$\text{RHS} = \left(\frac{1}{|\Omega|}\int_\Omega \sigma_{ik}\,\mathrm{d}\Omega\right)\left(\frac{1}{2|\Omega|}\int_{\partial\Omega} (u_i n_k + n_i u_k)\,\mathrm{d}\Omega\right)$$

substituting the linear displacement boundary condition, $\boldsymbol{u} = \boldsymbol{\mathcal{E}}\boldsymbol{x}$, we get,

$$= \left(\frac{1}{|\Omega|}\int_\Omega \sigma_{ik}\,\mathrm{d}\Omega\right)\left(\frac{1}{2|\Omega|}\int_{\partial\Omega} (\mathcal{E}_{ij}x_j n_k + \mathcal{E}_{kj}x_j n_i)\,\mathrm{d}\Omega\right)$$

and using integration by parts to obtain

$$= \left(\frac{1}{|\Omega|}\int_\Omega \sigma_{ik}\,\mathrm{d}\Omega\right)\left(\frac{1}{2|\Omega|}\int_{\Omega} \frac{\partial}{\partial x_k}(\mathcal{E}_{ij}x_j) + \frac{\partial}{\partial x_i}(\mathcal{E}_{kj}x_j)\,\mathrm{d}\Omega\right)$$

as $\mathcal{E}$ is constant,

$$= \left(\frac{1}{|\Omega|}\int_\Omega \sigma_{ik}\,\mathrm{d}\Omega\right)\left(\frac{1}{2|\Omega|}\int_{\Omega} \mathcal{E}_{ij}(\frac{\partial x_j}{\partial x_k}) + \mathcal{E}_{kj}(\frac{\partial x_j}{\partial x_i})\,\mathrm{d}\Omega\right)$$
$$= \left(\frac{1}{|\Omega|}\int_\Omega \sigma_{ik}\,\mathrm{d}\Omega\right)\left(\frac{1}{2|\Omega|}\int_{\Omega} \mathcal{E}_{ij}\delta_{jk} + \mathcal{E}_{kj}\delta_{ji}\,\mathrm{d}\Omega\right)$$

where δ_{ij} is the Kronecker delta

$$= \left(\frac{1}{|\Omega|}\int_\Omega \sigma_{ik}\,\mathrm{d}\Omega\right)\left(\frac{1}{2|\Omega|}\int_{\Omega} \mathcal{E}_{ik} + \mathcal{E}_{ki}\,\mathrm{d}\Omega\right)$$
$$= \left(\frac{1}{|\Omega|}\int_\Omega \sigma_{ik}\,\mathrm{d}\Omega\right)\left(\frac{1}{2}(\mathcal{E}_{ik} + \mathcal{E}_{ki})\right).$$

Returning to matrix notation, we now have,

$$\begin{aligned}\text{RHS} &= \left(\frac{1}{|\Omega|}\int_\Omega \boldsymbol{\sigma}\,\mathrm{d}\Omega\right) : \left(\frac{1}{2}(\mathcal{E}+\mathcal{E}^T)\right) \\ &= \frac{1}{|\Omega|}\int_\Omega \boldsymbol{\sigma} : \frac{1}{2}(\mathcal{E}+\mathcal{E}^T)\,\mathrm{d}\Omega\,.\end{aligned}$$

Using the definition of small strain, $\boldsymbol{\varepsilon} = \frac{1}{2}(\nabla\boldsymbol{u} + (\nabla\boldsymbol{u})^T)$ and noticing that $\nabla\boldsymbol{u} = \mathcal{E}$ and $(\nabla\boldsymbol{u})^T = \mathcal{E}^T$, we have $\boldsymbol{\varepsilon} = \frac{1}{2}(\mathcal{E}+\mathcal{E}^T)$. Therefore,

$$\text{RHS} = \frac{1}{|\Omega|}\int_\Omega \boldsymbol{\sigma} : \boldsymbol{\varepsilon}\,\mathrm{d}\Omega = \text{LHS}$$

thus Hill's condition is satisfied by the linear displacement boundary condition.

2.4.1 Bounding the results: The Reuss and Voigt bounds

Statistical data gathered from a number of tests on same-sized samples with different arrangements of fibres gives an array of material property values which may be used to find an averaged, effective elastic modulus, denoted as $\tilde{\mathbb{E}}^*$. This data can be utilised in the verification of the method used to find the effective material properties.

It is useful to have a way of bounding the results, for example by using the classical Reuss [23] and Voigt [29] bounds, derived as follows:

If the strain field over a domain is split into a volume average and a purely fluctuating part, it becomes: $\boldsymbol{\varepsilon} = \langle\boldsymbol{\varepsilon}\rangle_\Omega + \tilde{\boldsymbol{\varepsilon}}$. Thus, using the fact that the elastic modulus is symmetric and positive definite, it can be deduced that,

$$\begin{aligned}0 &\leq \int_\Omega \tilde{\boldsymbol{\varepsilon}} : \mathbb{E}\tilde{\boldsymbol{\varepsilon}}\;\mathrm{d}\Omega \\ &= \int_\Omega (\boldsymbol{\varepsilon} - \langle\boldsymbol{\varepsilon}\rangle_\Omega) : \mathbb{E}(\boldsymbol{\varepsilon} - \langle\boldsymbol{\varepsilon}\rangle_\Omega)\;\mathrm{d}\Omega\end{aligned}$$

expanding this we get,

$$0 \leq \int_{\Omega} \boldsymbol{\varepsilon} : \mathbb{E}\boldsymbol{\varepsilon} - 2\langle\boldsymbol{\varepsilon}\rangle_{\Omega} : \mathbb{E}\boldsymbol{\varepsilon} + \langle\boldsymbol{\varepsilon}\rangle_{\Omega} : \mathbb{E}\langle\boldsymbol{\varepsilon}\rangle_{\Omega} \, \mathrm{d}\Omega \,. \tag{2.53}$$

We notice that we can use a form of Hill's condition,

$$\langle\boldsymbol{\varepsilon}\rangle_{\Omega} : \mathbb{E}^{*}\langle\boldsymbol{\varepsilon}\rangle_{\Omega} = \frac{1}{|\Omega|} \int_{\Omega} \boldsymbol{\varepsilon} : \mathbb{E}\boldsymbol{\varepsilon} \mathrm{d}\Omega \,.$$

For the second term we use,

$$\langle\boldsymbol{\sigma}\rangle_{\Omega} = \frac{1}{|\Omega|} \int_{\Omega} \mathbb{E}\boldsymbol{\varepsilon} \mathrm{d}\Omega$$

and finally, for the third term we use,

$$\langle\mathbb{E}\rangle_{\Omega} = \frac{1}{|\Omega|} \int_{\Omega} \mathbb{E} \mathrm{d}\Omega \,. \tag{2.54}$$

Thus the inequality in (2.53) becomes,

$$0 \leq \left(\langle\boldsymbol{\varepsilon}\rangle_{\Omega} : \mathbb{E}^{*}\langle\boldsymbol{\varepsilon}\rangle_{\Omega} - 2\langle\boldsymbol{\varepsilon}\rangle_{\Omega} : \langle\boldsymbol{\sigma}\rangle_{\Omega} + \langle\boldsymbol{\varepsilon}\rangle_{\Omega} : \langle\mathbb{E}\rangle_{\Omega}\langle\boldsymbol{\varepsilon}\rangle_{\Omega} \right) |\Omega|$$

which is then,

$$0 \leq \big(\langle\boldsymbol{\varepsilon}\rangle_{\Omega} : (\langle\mathbb{E}\rangle_{\Omega} - \mathbb{E}^{*})\langle\boldsymbol{\varepsilon}\rangle_{\Omega} \big) |\Omega| \,. \tag{2.55}$$

Similarly, for $\boldsymbol{\sigma} = \langle\boldsymbol{\sigma}\rangle_{\Omega} + \tilde{\boldsymbol{\sigma}}$,

$$\begin{aligned} 0 &\leq \int_{\Omega} \tilde{\boldsymbol{\sigma}} : \mathbb{E}^{-1}\tilde{\boldsymbol{\sigma}} \mathrm{d}\Omega \\ &= \int_{\Omega} (\boldsymbol{\sigma} - \langle\boldsymbol{\sigma}\rangle_{\Omega}) : \mathbb{E}^{-1}(\boldsymbol{\sigma} - \langle\boldsymbol{\sigma}\rangle_{\Omega}) \, \mathrm{d}\Omega \end{aligned} \tag{2.56}$$

expanding,

$$= \int_{\Omega} \boldsymbol{\sigma} : \mathbb{E}^{-1}\boldsymbol{\sigma} - 2\langle\boldsymbol{\sigma}\rangle_{\Omega} : \mathbb{E}^{-1}\boldsymbol{\sigma} + \langle\boldsymbol{\sigma}\rangle_{\Omega} : \mathbb{E}^{-1}\langle\boldsymbol{\sigma}\rangle_{\Omega} \, \mathrm{d}\Omega \,.$$

Now, for the first term using,

$$\langle \boldsymbol{\sigma} \rangle_{\Omega} \colon \mathbb{E}^{*} \langle \boldsymbol{\sigma} \rangle_{\Omega} = \frac{1}{|\Omega|} \int_{\Omega} \boldsymbol{\sigma} \colon \mathbb{E} \boldsymbol{\sigma} \, \mathrm{d}\Omega$$

for the second term we use,

$$\langle \boldsymbol{\varepsilon} \rangle_{\Omega} = \mathbb{E}^{*-1} \langle \boldsymbol{\sigma} \rangle_{\Omega} \tag{2.57}$$

and using equation (2.54) for the third term, we get,

$$0 \leq \left(\langle \boldsymbol{\sigma} \rangle_{\Omega} \colon \mathbb{E}^{*-1} \colon \langle \boldsymbol{\sigma} \rangle_{\Omega} - 2 \langle \boldsymbol{\varepsilon} \rangle_{\Omega} \colon \langle \boldsymbol{\sigma} \rangle_{\Omega} + \langle \boldsymbol{\sigma} \rangle_{\Omega} \colon \langle \mathbb{E}^{-1} \rangle_{\Omega} \colon \langle \boldsymbol{\sigma} \rangle_{\Omega} \right) |\Omega| \, .$$

So,

$$0 \leq \left(\langle \boldsymbol{\sigma} \rangle_{\Omega} \colon \left(\langle \mathbb{E}^{-1} \rangle_{\Omega} - \mathbb{E}^{*-1} \right) \colon \langle \boldsymbol{\sigma} \rangle_{\Omega} \right) |\Omega| \, . \tag{2.58}$$

Thus the effective value is bounded,

$$\langle \mathbb{E}^{-1} \rangle_{\Omega}^{-1} \leq \mathbb{E}^{*} \leq \langle \mathbb{E} \rangle_{\Omega} \tag{2.59}$$

where the value to the left of the inequality is known as the Reuss bound and that to the right of the inequality is the Voigt bound.

2.5 Partitioning of domain/bounding results

Consider a large sample (assumed to be too large a sample to be computationally feasible) that is partitioned to form N subdomains as shown in Figure 2.8, where each subdomain comprises a single RVE, such that,

$$\Omega = \cup_{K=1}^{N} \Omega_K \, . \tag{2.60}$$

If the boundary value problem is solved on each subdomain, Ω_K, with the loading $\mathbf{u}|_{\partial\Omega_K} = \mathcal{E} \cdot \mathbf{x}$ (linear displacement boundary constraint where the strain field must include both volumetric and dilatational components), the following properties can be obtained, as shown by Huet [11],

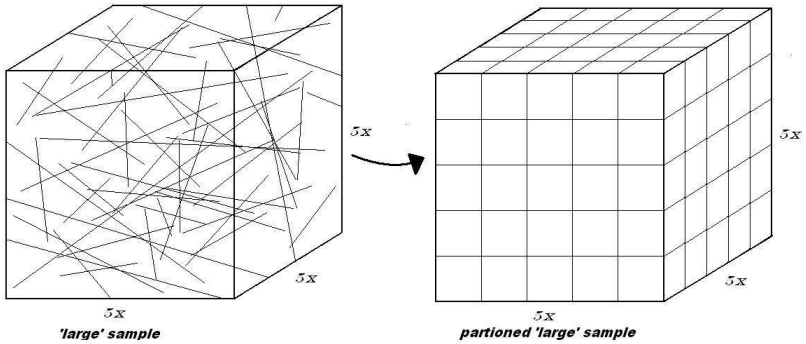

Fig. 2.8: The partitioning of a "large" domain into 125 subdomains

$$\langle \tilde{\boldsymbol{\sigma}} \rangle_{\Omega_K} := \tilde{\mathbb{E}}^*_K : \langle \tilde{\boldsymbol{\varepsilon}} \rangle_{\Omega_K}, \quad \tilde{\mathbb{E}}^* := \sum_{K=1}^{N} \mathbb{E}^*_K \frac{|\Omega_K|}{|\Omega|} \tag{2.61}$$

$$\langle \mathbb{E}^{-1} \rangle^{-1}_{\Omega} \leq \mathbb{E}^* \leq \tilde{\mathbb{E}}^* \leq \langle \mathbb{E} \rangle_{\Omega} \tag{2.62}$$

$$\mathbf{u} := \tilde{\mathbf{u}}_1|_{\overline{\Omega}_1} + \tilde{\mathbf{u}}_2|_{\overline{\Omega}_2} \ldots \tilde{\mathbf{u}}_N|_{\overline{\Omega}_N} . \tag{2.63}$$

The notation $\tilde{\varphi}$ indicates the aggregate value of the relevant quantity φ over the subdomains, thus $\tilde{\mathbb{E}}^*_K$ denotes the aggregate of the results as shown in Equation (2.61). These equations help to bound the problem, for example, Equation (2.62) shows that for linear displacement tests the response for the large sample is bounded from above by the averaged effective responses. If this process were to be repeated for constant traction tests it can be shown that the response for the large sample is bounded from below by the averaged effective responses. This means that the linear displacement boundary condition gives an "over-stiff" response, and the constant traction boundary condition an "under-stiff" response. These results thus give upper and lower bounds for the problem and can be used to tighten the bounds detailed in Section 4.2.2.

2.5.1 Proof of Equations (2.61) to (2.63)

Equations (2.61) to (2.63) can be proved using the principle of minimum potential energy as follows.

The large domain consists of the union of N smaller domains, $\Omega = \cup_{K=1}^{N} \Omega_K$. If $\mathbf{u}$ is the exact solution to the problem on the large domain, the variational boundary value problem is, find the displacement field, $\mathbf{u}$, $\mathbf{u}|_{\Gamma_u} = \mathbf{d}$, such that

$$\int_{\Omega} \nabla \mathbf{w} \colon \mathbb{E} \nabla \mathbf{u} \, \mathrm{d}\Omega = \int_{\Omega} \mathbf{f} \cdot \mathbf{w} \, \mathrm{d}\Omega + \int_{\Gamma_t} \mathbf{t} \cdot \mathbf{w} \, \mathrm{dA} \qquad \text{s.t.} \quad \mathbf{w}|_{\Gamma_u} = 0 \,. \tag{2.64}$$

If $\tilde{\mathbf{u}}_K$ is the solution to the problem on subdomain K, and $\partial\Omega_K$ denotes the boundary of Ω_K, then the variational boundary value problem on subdomain K is: find $\tilde{\mathbf{u}}_K$, $\tilde{\mathbf{u}}_K|_{\partial\Omega \cap (\Omega \cup \Gamma_u)} = \mathbf{U}$, such that,

$$\int_{\Omega_K} \nabla \mathbf{w}_K \colon \tilde{\boldsymbol{\sigma}}_K \, \mathrm{d}\Omega = \int_{\Omega_K} \mathbf{f} \cdot \mathbf{w}_K \, \mathrm{d}\Omega + \int_{\partial\Omega_K \cap \Gamma_t} \mathbf{t} \cdot \mathbf{w}_K \, \mathrm{dA} \qquad \text{s.t.} \quad \mathbf{w}_K|_{\partial\Omega_K \cap (\Omega \cup \Gamma_u)} = 0 \,. \tag{2.65}$$

The assembly of the solutions to the BVP on the individual subdomains, $\tilde{\mathbf{u}}$, gives an approximation to the exact solution, $\mathbf{u}$, when assembled as follows,

$$\tilde{\mathbf{u}} \colon = \tilde{\mathbf{u}}_1|_{\Gamma_1} + \ldots + \tilde{\mathbf{u}}_N|_{\Gamma_N} \,. \tag{2.66}$$

For the elastic potential of $\mathbf{u}$ and $\mathbf{w}$, defined as,

$$\mathcal{J}(\mathbf{u}) = \frac{1}{2}\mathcal{B}(\mathbf{u}, \mathbf{u}) - f(\mathbf{u}) \qquad \text{and:} \tag{2.67}$$

$$\mathcal{J}(\mathbf{w}) = \frac{1}{2}\mathcal{B}(\mathbf{w}, \mathbf{w}) - f(\mathbf{w}) \tag{2.68}$$

where $\mathcal{B}(\cdot)$ is a bilinear form expressing the elastic energy in the system and $f(\cdot)$ represents the external forces [12]. So Equation (2.68), for example, is defined as,

$$\frac{1}{2} \int_{\Omega} \nabla \boldsymbol{w} \colon \mathbb{E} \colon \nabla \boldsymbol{w} \, \mathrm{d}\Omega - \int_{\Omega} \boldsymbol{w} \, \mathrm{d}\boldsymbol{\Omega} - \int_{\boldsymbol{\Gamma_t}} \boldsymbol{t} \cdot \boldsymbol{w} \, \mathrm{dA} \tag{2.69}$$

The following norm is defined for any kinematically admissible function,

$$
\begin{aligned}
0 \leq \|\mathbf{u}-\mathbf{w}\|^2_{E(\Omega)} :\ &= \mathcal{B}(\mathbf{u}-\mathbf{w},\mathbf{u}-\mathbf{w}) \\
&= \mathcal{B}(\boldsymbol{w},\boldsymbol{w}) - 2\mathcal{B}(\boldsymbol{u},\boldsymbol{w}) + \mathcal{B}(\boldsymbol{u},\boldsymbol{u}) \\
&= \mathcal{B}(\boldsymbol{w},\boldsymbol{w}) - \mathcal{B}(\boldsymbol{u},\boldsymbol{u}) - 2\underbrace{\mathcal{B}(\boldsymbol{u},\boldsymbol{w})}_{f(\boldsymbol{w})} + 2\underbrace{\mathcal{B}(\boldsymbol{u},\boldsymbol{u})}_{f(\boldsymbol{u})} \\
&= \mathcal{B}(\boldsymbol{w},\boldsymbol{w}) - 2f(\boldsymbol{w}) - [\mathcal{B}(\boldsymbol{u},\boldsymbol{u}) - 2f(\boldsymbol{u})] \\
&= 2\mathcal{J}(\boldsymbol{w}) - 2\mathcal{J}(\boldsymbol{u})\,. \qquad (2.70)
\end{aligned}
$$

Equation (2.70) is the Principle of Minimum Potential Energy (PMPE),which can then be expressed as,

$$\mathcal{J}(\boldsymbol{u}) \leq \mathcal{J}(\boldsymbol{w})\,. \qquad (2.71)$$

That is, the exact solution is less than or equal to any arbitrary solution. If $\boldsymbol{U}$ is defined as $\boldsymbol{U} := \mathcal{E}.\mathbf{x}$, we choose $\mathbf{w} = \boldsymbol{U}$, so that $\tilde{\mathbf{u}}$ is also kinematically admissable, and using Equation (2.71),

$$
\begin{aligned}
\|\mathbf{u}-\tilde{\mathbf{u}}\|^2_{E(\Omega)} &= 2(\mathcal{J}(\tilde{\mathbf{u}}) - \mathcal{J}(\mathbf{u})) \\
&= 2(\mathcal{J}(\tilde{\mathbf{u}}) - \mathcal{J}(\mathbf{w})) + \|\mathbf{u}-\mathbf{w}\|^2_{E(\Omega)}\,. \qquad (2.72)
\end{aligned}
$$

$\tilde{\boldsymbol{u}}_K$ minimises the subdomain potential energy function $f_K(\cdot)$ as it is a solution to the BVP over the subdomain Ω_K, therefore,

$$\mathcal{J}(\mathbf{w}) \geq \mathcal{J}(\tilde{\mathbf{u}}) \qquad \text{where:} \qquad (2.73)$$

$$\mathcal{J}(\mathbf{w}) = \sum_{K=1}^{N} \mathcal{J}_K(\mathbf{w}) \qquad \text{and} \qquad \mathcal{J}(\tilde{\mathbf{u}}) = \sum_{K=1}^{N} \mathcal{J}_K(\tilde{\mathbf{u}}_K) \qquad (2.74)$$

and from (2.72), we find that,

$$\|\boldsymbol{u}-\tilde{\boldsymbol{u}}\|^2_{E(\Omega)} \leq \|\boldsymbol{u}-\boldsymbol{w}\|^2_{E(\Omega)}\,. \qquad (2.75)$$

So for $\boldsymbol{w} = \boldsymbol{U}$,

$$\|\boldsymbol{u} - \tilde{\boldsymbol{u}}\|^2_{E(\Omega)} \leq \|\boldsymbol{u} - \boldsymbol{U}\|^2_{E(\Omega)} \,. \tag{2.76}$$

Expanding the right hand side of the above inequality and using Equation (2.59), we get,

$$\|\boldsymbol{u} - \boldsymbol{U}\|^2_{E(\Omega)} = \mathcal{E} \colon \langle \mathbb{E} \rangle - \mathbb{E}^* \mathcal{E} | \Omega | \leq \mathcal{E} \colon \langle \mathbb{E} \rangle - \langle \mathbb{E}^{-1} \rangle^{-1} \mathcal{E} | \Omega | \,. \tag{2.77}$$

By definition we have,

$$2\mathcal{J}(\mathbf{u}) = \mathcal{E} \colon \mathbb{E}^* \colon \mathcal{E} | \Omega | \tag{2.78}$$

$$2\mathcal{J}_K(\tilde{\mathbf{u}}) = \mathcal{E} \colon \tilde{\mathbb{E}}^*_K \colon \mathcal{E} | \Omega_K | \Rightarrow 2\mathcal{J}(\tilde{\mathbf{u}}) = \mathcal{E} \colon \tilde{\mathbb{E}}^* \colon \mathcal{E} | \Omega | \tag{2.79}$$

$$2\mathcal{J}(\mathbf{w}) = \mathcal{E} \colon \langle \mathbb{E}^* \rangle \colon \mathcal{E} | \Omega | \,. \tag{2.80}$$

Now expanding the left hand side of Equation (2.76) and using Equation (2.76) we get,

$$\boldsymbol{\varepsilon} \colon (\tilde{\mathbb{E}}^* - \mathbb{E}^*) \boldsymbol{\varepsilon} | \Omega | \leq \boldsymbol{\varepsilon} \colon (\tilde{\mathbb{E}}^* - \langle \mathbb{E}^{-1} \rangle^{-1}_{\Omega})) \boldsymbol{\varepsilon} | \Omega | \,. \tag{2.81}$$

Thus the Reuss-Voigt bounds from Section 4.2.2 are tightened. These bounds as well as the statistical analyses can be used to verify the results from the linear displacement tests on the subdomain RVEs. While, in this thesis, the problem is for equally sized samples with a random fibre distribution, the theory presented here can be applied to an irregular partitioning of the large sample with any microstructure.

3

The finite element method

In this thesis the finite element method is used to solve the system of partial differential equations that govern the problem. This chapter starts with a summary of the finite element method (FEM) for the application of linear elasticity in a small strain context, this section is based on the theory presented by [5] and [22]. The FEM was used to solve the problem presented for this thesis. The enforcement of boundary constraints via lagrange multipliers and the penalty method is introduced in Chapter 2. The finite element implementation of these boundary constraint enforcement options is presented in this chapter and the results of the implementations are discussed.

3.1 The finite element method for small strain linear elasticity

In Section 2.1 the weak form of the boundary value problem is developed; the equation is reproduced here for convenience,

$$\int_{\Omega} (\nabla_S^T \boldsymbol{w})^T \mathbf{D} \nabla_S \boldsymbol{u} \mathrm{dV} = \int_{\Omega} \boldsymbol{w}^T \boldsymbol{b} \mathrm{dV} + \int_{\Gamma_t} \boldsymbol{w}^T \bar{t} \mathrm{dA} \tag{3.1}$$

where $\mathbf{D}$ is the elasticity modulus defined in equation (2.41). The finite element method finds an approximate solution to the problem using the Galerkin method.

An approximate displacement solution, $\boldsymbol{u}$, can be defined as a linear combination of shape or basis functions as follows,

$$\boldsymbol{u} = \boldsymbol{N}\boldsymbol{d} \tag{3.2}$$

where the $3 \times 3R$ basis functions, $\boldsymbol{N}$ and the $3R \times 1$ vector of unknowns, $\boldsymbol{d}$ are defined as,

$$\boldsymbol{N} = \begin{bmatrix} N_1 & 0 & 0 & N_2 & 0 & 0 \cdots & N_R & 0 & 0 \\ 0 & N_1 & 0 & 0 & N_2 & 0 \cdots & 0 & N_R & 0 \\ 0 & 0 & N_1 & 0 & 0 & N_2 \cdots & 0 & 0 & N_R \end{bmatrix} \quad , \quad \boldsymbol{d} = \begin{bmatrix} d_1 \, d_2 \cdots \, d_{3R} \end{bmatrix}^T \, . \tag{3.3}$$

The arbitrary displacement can likewise be expressed as $\boldsymbol{w} = \boldsymbol{N}\boldsymbol{q}$. The small strain tensor, defined in Voigt notation in Section 2.1 and expressed as,

$$\boldsymbol{\varepsilon}(\boldsymbol{u}) = \begin{bmatrix} \frac{\partial u_1}{\partial x} \\ \frac{\partial u_2}{\partial y} \\ \frac{\partial u_3}{\partial z} \\ \frac{\partial u_1}{\partial y} + \frac{\partial u_2}{\partial x} \\ \frac{\partial u_1}{\partial z} + \frac{\partial u_3}{\partial x} \\ \frac{\partial u_2}{\partial z} + \frac{\partial u_3}{\partial y} \end{bmatrix} = \nabla_S^T \boldsymbol{u} \tag{3.4}$$

can, using the definition of the approximate solution, be expressed as,

$$\boldsymbol{\varepsilon}(\boldsymbol{u}) = \nabla_S^T \boldsymbol{u} = \nabla_S^T \boldsymbol{N}\boldsymbol{d} = \boldsymbol{B}\boldsymbol{d} \tag{3.5}$$

$$\text{where} \qquad \boldsymbol{B} = \nabla_S^T \boldsymbol{N} \, . \tag{3.6}$$

Now the preceding quantities are substituted into the weak form, Equation (2.33) to obtain,

$$\boldsymbol{q}^T \left(\int_\Omega \boldsymbol{B}^T \boldsymbol{D} \boldsymbol{B} \;\; \mathrm{dV} \right) \boldsymbol{d} = \boldsymbol{q}^T \left(\int_\Omega \boldsymbol{N}^T \overline{\boldsymbol{b}} \;\; \mathrm{dV} + \int_{\Gamma_N} \boldsymbol{N}^T \overline{\boldsymbol{t}} \;\; \mathrm{dA} \right) . \tag{3.7}$$

By defining the stiffness matrix $\boldsymbol{K}$ and force vector $\boldsymbol{F}$,

$$\boldsymbol{K} = \int_{\Omega} \boldsymbol{B}^T \boldsymbol{D} \boldsymbol{B} \, \mathrm{dV} \qquad , \qquad \boldsymbol{F} = \int_{\Omega} \boldsymbol{N}^T \overline{\boldsymbol{b}} \, \mathrm{dV} + \int_{\Gamma_N} \boldsymbol{N}^T \overline{\boldsymbol{t}} \, \mathrm{dA} \tag{3.8}$$

the matrix problem to be solved can be expressed as,

$$\boldsymbol{K}\boldsymbol{d} = \boldsymbol{F} \tag{3.9}$$

or, as $\boldsymbol{K}$ is invertible,

$$\boldsymbol{d} = \boldsymbol{K}^{-1}\boldsymbol{F} \, . \tag{3.10}$$

Now an approximation to the displacement and the stress may be found using,

$$\boldsymbol{u} = \boldsymbol{N}\boldsymbol{d} \qquad \text{and} \qquad \boldsymbol{\sigma} = \boldsymbol{D}\boldsymbol{\varepsilon} = \boldsymbol{D}\boldsymbol{B}\boldsymbol{d} \, . \tag{3.11}$$

3.1.1 Implementing the finite element method

The finite element method completes the above process such that the definition of $\boldsymbol{N}$ and increasing the accuracy of $\boldsymbol{u}$ is simple.

The domain Ω is partitioned into P finite subdomains, called elements, $\Omega_1, \Omega_2 \cdots \Omega_P$. Adjacent elements share parts of boundaries such that the entire unpartitioned domain is filled, while these elements never overlap, that is,

$$\cup_{j=1}^{P} \overline{\Omega}_j = \overline{\Omega} \qquad \text{(elements fill domain)} \tag{3.12}$$

$$\Omega_i \cap \Omega j = \varnothing \quad \text{for} \quad i \neq j \qquad \text{(no overlapping)} \, . \tag{3.13}$$

Nodes are assigned to the elements, with at least a node at each vertex (the elements have straight edges). More nodes can be added, for example midway along an element boundary, for increased accuracy in the approximation. The combination of nodes and elements makes up what is known as the finite element mesh, an example of which is shown in Figure 3.1.

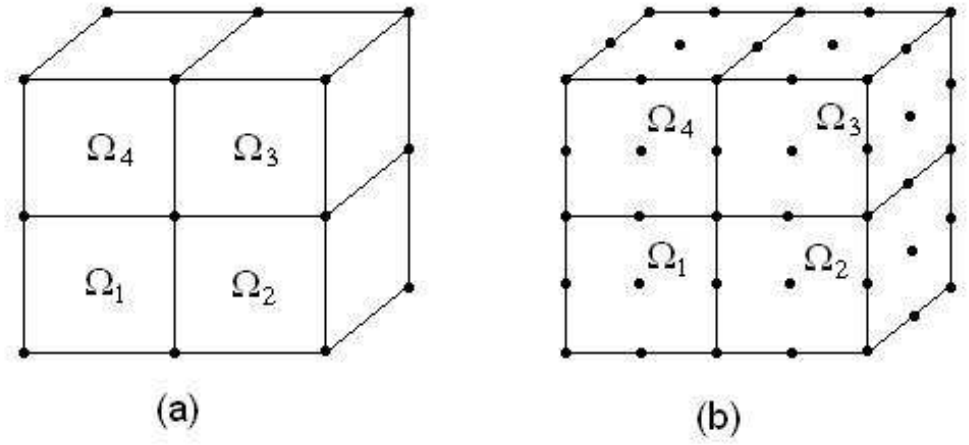

Fig. 3.1: Finite element meshes with a) nodes only at vertices and b) additional nodes

A basis or shape function, N_i exists for every node. N_i is equal to one at node i and zero at every other node and all the shape functions are continuous throughout the domain. Thus N_i is only non-zero on elements connected to node i. The local basis function, that is the part of N_i on element Γ_e, is denoted $N_i^{(e)}$ and is a polynomial of degree $k \geq 1$, thus, for the global basis function,

$$N_i(x_j) = \begin{cases} 1 & \text{if} \quad i = j \\ 0 & \text{otherwise} \end{cases} \tag{3.14}$$

and for the local basis function,

$$N_i^{(e)}(x_j) = \begin{cases} 1 & \text{if} \quad i = j \\ 0 & \text{otherwise} \end{cases} . \tag{3.15}$$

These properties are illustrated in Figure 3.2, where they are shown for a 2-dimensional quadrilateral mesh where the basis function is bilinear locally.

Now equations (3.2) and (3.14) are used to get,

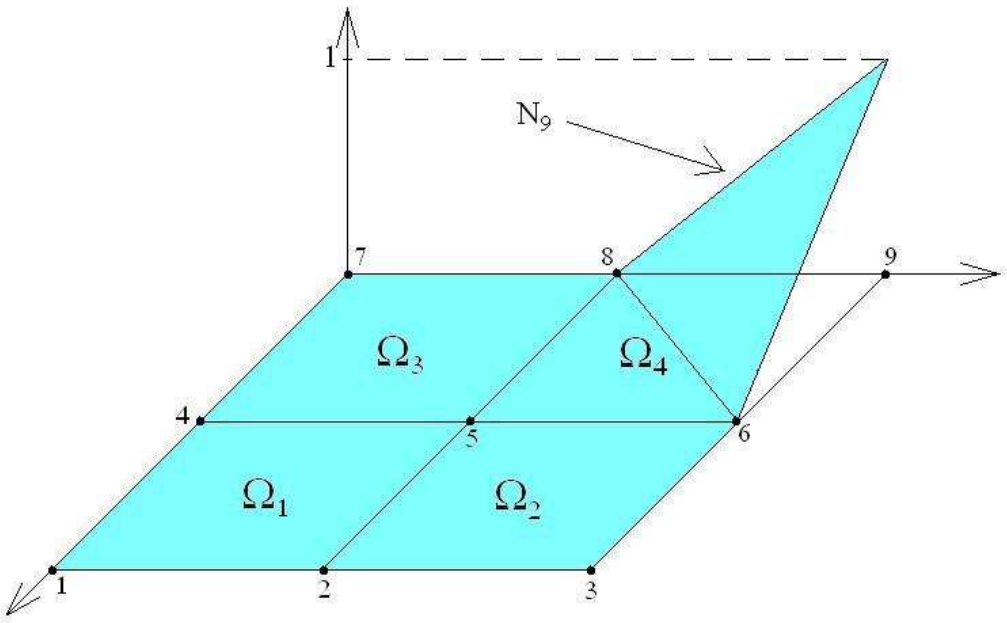

Fig. 3.2: The shape function N_9 for global node number 9

$$\boldsymbol{u}(x_j) = \sum_{i=1}^{\text{no. nodes}} d_i N_i(x_j) = d_j \tag{3.16}$$

meaning that the value of $\boldsymbol{u}$ at node j is d_j.

From $\boldsymbol{F} = \boldsymbol{K}\boldsymbol{d}$, $\boldsymbol{K}$ can be written as an assembly of the element quantities as follows,

$$\boldsymbol{K} = \int_\Omega \boldsymbol{B}^T \boldsymbol{D} \boldsymbol{B} \mathrm{dV} \tag{3.17}$$

$$= \sum_{e=1}^{E} \left(\int_\Omega \boldsymbol{B}^{eT} \boldsymbol{D} \boldsymbol{B}^e \mathrm{dV} \right) \tag{3.18}$$

and the element stiffness matrix, $\boldsymbol{K}^e$, is defined as the parenthesised quantity. Similarly for $\boldsymbol{F}$,

$$\boldsymbol{F} = \int_{\Omega} \boldsymbol{N}^T \overline{\boldsymbol{b}} \mathrm{dV} + \int_{\Gamma_N} \boldsymbol{N}^T \overline{\boldsymbol{t}} \mathrm{dA} \tag{3.19}$$

$$= \sum_{e=1}^{E} \left(\int_{\Omega_e} \boldsymbol{N}^{eT} \overline{\boldsymbol{b}} \mathrm{dV} + \int_{\Gamma_N^e} \boldsymbol{N}^{eT} \overline{\boldsymbol{t}} \mathrm{dA} \right) \tag{3.20}$$

where the element force vector, $\boldsymbol{F}^e$ is the quantity in brackets. The property of the basis functions shown in equation (3.14) results in the stiffness matrix containing zero value entries, that is, $K_{ij}^e = 0$ if the nodes i, j are not on Ω_e. It is then possible to number the nodes such that $\boldsymbol{K}$ is banded, so that the inversion of the matrix is less computationally strenuous.

The simplest element type is one that yields piecewise-linear approximations to the displacement field. This linear element would have only vertex nodes and the accuracy of the approximation to $\boldsymbol{u}$ could then be increased by adding extra nodes to the elements. An example of a finite element mesh using linear elements in 2D is shown in Figure 3.3. At element level a convenient numbering system for the element nodes

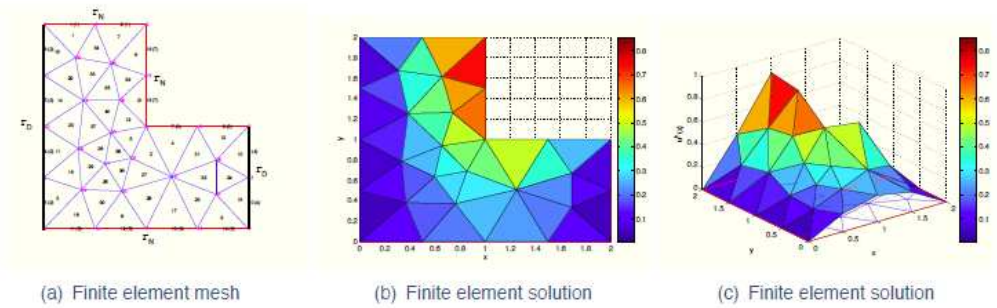

Fig. 3.3: Finite element mesh using a piecewise-linear approximation

is anti-clockwise starting from 1. $\boldsymbol{K}^{(e)}$ and $\boldsymbol{F}^{(e)}$ can then be evaluated and their components correctly added to the corresponding global quantities. This process is known as assembly.

The shape functions are defined for an isoparametric element, with the coordinate system (ξ, η, ζ), in which $\hat{\Omega}$ is defined. As shown in Figure 3.4, the isoparametric element is an eight noded cube. The basis function is defined here and then simply mapped to the reference element as follows,

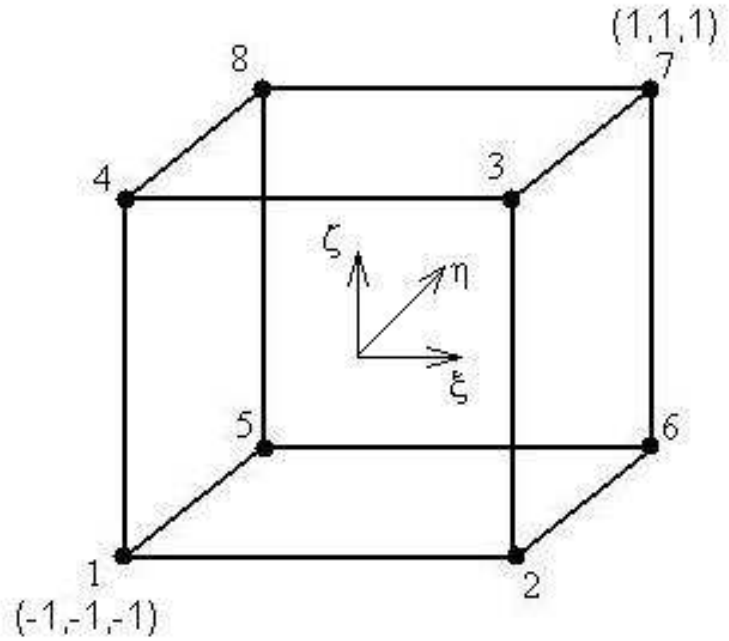

Fig. 3.4: The eight noded brick isoparametric element and the corresponding reference element

$$x = \sum_{A=1}^{8} x_A N_A \tag{3.21}$$

$$y = \sum_{A=1}^{8} y_A N_A \tag{3.22}$$

$$z = \sum_{A=1}^{8} z_A N_A \,. \tag{3.23}$$

Thus each point $\xi \in \hat{\Omega}$ is mapped to $x \in \Omega_e$. $\hat{N}(\xi, \eta, \zeta)$ satisfy Equation (3.14), and, according to the node numbering shown in 3.4 are given as,

$$\begin{aligned}
\hat{N}_1(\xi,\eta,\zeta) &= \frac{1}{8}(1-\xi)(1-\eta)(1-\zeta) \quad ; \quad \hat{N}_2(\xi,\eta,\zeta) = \frac{1}{8}(1+\xi)(1-\eta)(1-\zeta) \\
\hat{N}_3(\xi,\eta,\zeta) &= \frac{1}{8}(1+\xi)(1-\eta)(1+\zeta) \quad ; \quad \hat{N}_4(\xi,\eta,\zeta) = \frac{1}{8}(1-\xi)(1-\eta)(1+\zeta) \\
\hat{N}_5(\xi,\eta,\zeta) &= \frac{1}{8}(1-\xi)(1+\eta)(1-\zeta) \quad ; \quad \hat{N}_6(\xi,\eta,\zeta) = \frac{1}{8}(1+\xi)(1+\eta)(1-\zeta) \\
\hat{N}_7(\xi,\eta,\zeta) &= \frac{1}{8}(1+\xi)(1+\eta)(1+\zeta) \quad ; \quad \hat{N}_8(\xi,\eta,\zeta) = \frac{1}{8}(1-\xi)(1+\eta)(1+\zeta)\,.
\end{aligned}$$

A numerical approximation to the integrals forming $\boldsymbol{F}^{(e)}$ and $\boldsymbol{K}^{(e)}$ is now required. The general approach to numerical integration is to evaluate the function at chosen sampling points within the domain and combine this value with specific weights, one for each sampling point. Then, for $\hat{\xi}_l$ representing the sampling points, W_l the weights and r equalling the order of the numerical integration,

$$\int_{\hat{\Omega}} f(\xi)\mathrm{d}\xi \simeq \sum_{l=1}^{r} W_l f(\hat{\xi}_l) \tag{3.24}$$

In this thesis the Gauss quadrature is used for the numerical integration, the integration point location and the corresponding weights are shown in Table 3.1. A polynomial of degree $2n-1$ will be integrated exactly by an integration rule of order n.

Table 3.1: Position of Gauss points and corresponding weights

no. Gauss Points	Location	Weights
1	0	2
2	$+/-0.5773502692$	1
3	$+/-0.7745966692$	0.5555555556
	0	0.8888888889

3.2 Implementation of boundary condition enforcements

In Chapter 2 two methods of enforcing the boundary contraints are presented. The finite element implementation of these methods is presented in the following section.

3.2.1 Lagrange multipliers

In Chapter 2 positive and negative boundaries were defined on the domain. According to these the periodic displacements and anti-periodic tractions are stated with the inclusion of a lagrange multiplier π, as

$$[(\mathbf{u}^+ - \mathbf{u}^-) - \mathcal{E}(\mathbf{x}^+ - \mathbf{x}^-)]\pi = \mathbf{0}, \qquad \mathbf{t}^+ + \mathbf{t}^- = \mathbf{0}\,.$$

For the discretised problem this equation becomes

$$\mathbf{u}(\overline{\mathbf{x}}^+) - \mathbf{u}(\overline{\mathbf{x}}^-) = \mathcal{E}[\overline{\mathbf{x}}^+ - \overline{\mathbf{x}}^+] \qquad \mathbf{t}(\overline{\mathbf{x}}^+) + \mathbf{t}(\overline{\mathbf{x}}^-) = \mathbf{0} \tag{3.25}$$

where the superscripts + and − denote quantities on the positive or negative boundaries as defined in Figure 3.5. Equation 3.25 can be represented in the following way,

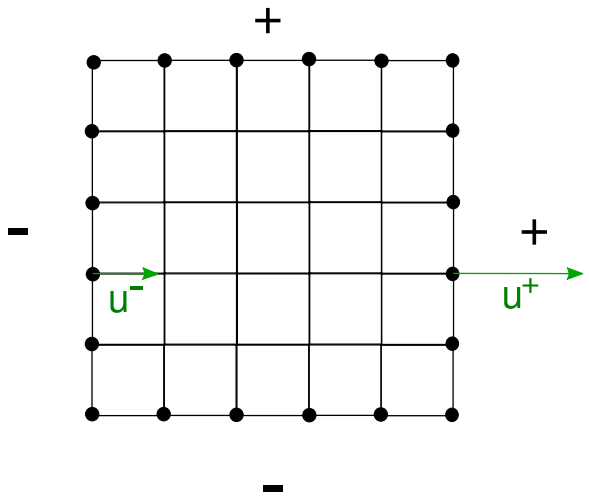

Fig. 3.5: Meshed RVE with positive (+) boundaries and corresponding negative (-) boundaries

$$\mathbb{P}_q \mathbf{u_b} = \mathbb{Q}_q^T \mathcal{E} \quad q = 1 \ldots P \tag{3.26}$$

where $\mathbb{P}_q$ forms a link topology matrix for the node pair q and,

$$\mathbb{Q}_q = \mathbb{D}_q^+ - \mathbb{D}_q^-, \qquad \text{where:} \qquad \mathbb{D}_q = \frac{1}{2} \begin{bmatrix} 2x_1 & 0 \\ 0 & 2x_2 \\ x_2 & x_1 \end{bmatrix} . \tag{3.27}$$

The three equations to be solved are,

$$\boldsymbol{F}_a(\boldsymbol{u}) = \mathbf{0} \tag{3.28}$$

$$\boldsymbol{F}_b(\boldsymbol{u}) - \mathbb{P}^T \pi = \mathbf{0} \tag{3.29}$$

$$\mathbb{P}\boldsymbol{u}_b - \mathbb{Q}^T \mathcal{E} = \mathbf{0} \,. \tag{3.30}$$

where $\boldsymbol{F}_a$ and $\boldsymbol{F}_b$ are the internal and external forces respectively.

If $\boldsymbol{u}$, $\boldsymbol{K}$ and $\boldsymbol{F}$ from Section 3.1 are partitioned such that,

$$\boldsymbol{u} = \begin{Bmatrix} \boldsymbol{u}_a \\ \boldsymbol{u}_b \end{Bmatrix} \tag{3.31}$$

$$\boldsymbol{F} = \begin{Bmatrix} \boldsymbol{F}_a \\ \boldsymbol{F}_b \end{Bmatrix} \tag{3.32}$$

$$\boldsymbol{K} = \begin{bmatrix} \boldsymbol{K}_{aa} & \boldsymbol{K}_{ab} \\ \boldsymbol{K}_{ba} & \boldsymbol{K}_{bb} \end{bmatrix} \tag{3.33}$$

where the subscript a is for internal nodes and subscript b is for those on the boundary. Thus we obtain,

$$\boldsymbol{F}_a + \boldsymbol{K}_{aa}\boldsymbol{u}_a + \boldsymbol{K}_{ab}\boldsymbol{u}_b = \mathbf{0} \tag{3.34}$$

$$\boldsymbol{F}_b - \mathbb{P}^T \pi + \boldsymbol{K}_{ba}\boldsymbol{u}_a + \boldsymbol{K}_{bb}\boldsymbol{u}_b - \mathbb{P}^T \pi = \mathbf{0} \tag{3.35}$$

$$\mathbb{P}\boldsymbol{u}_b - \mathbb{Q}^T \mathcal{E} + \mathbb{P}\Delta\boldsymbol{u}_b - \mathbb{Q}^T \Delta\mathcal{E} = \mathbf{0} \,. \tag{3.36}$$

The matrix problem to be solved is then,

$$\begin{bmatrix} \boldsymbol{K}_{aa} & \boldsymbol{K}_{ab} & \mathbf{0} \\ \boldsymbol{K}_{ba} & \boldsymbol{K}_{bb} & \mathbb{P}^T \\ \mathbf{0} & \mathbb{P} & \mathbf{0} \end{bmatrix} \begin{Bmatrix} \boldsymbol{u}_a \\ \boldsymbol{u}_b \\ \pi \end{Bmatrix} = \begin{Bmatrix} \boldsymbol{F}_a \\ \boldsymbol{F}_b \\ \mathbb{Q}^T \mathcal{E} \end{Bmatrix} . \tag{3.37}$$

The macroscopic stress $\boldsymbol{\sigma}$ is defined as,

$$\langle \boldsymbol{\sigma} \rangle = \frac{1}{|V|} \int_V \boldsymbol{\sigma} \ \mathrm{dV}$$

using the divergence theorem we can re-write this as,

$$\boldsymbol{\sigma} := \frac{1}{V} \int_{\partial\Omega} \mathrm{sym}[\mathbf{t} \otimes \mathbf{x}] \ dA \tag{3.38}$$

now, as $\mathbf{t} \ dA \to \pi$ in the discrete setting, we obtain,

$$\boldsymbol{\sigma} = \frac{1}{V} \sum_{q=1}^{P} \mathrm{sym}[\pi_{\mathbf{q}} \otimes [\![\mathbf{x}_{\mathbf{q}}]\!]] \quad = \quad \frac{1}{V} \sum_{q=1}^{P} \mathbb{Q}_q \pi_{\mathbf{q}} \tag{3.39}$$

where $[\![(\cdot)]\!] = (\cdot)^+ - (\cdot)^-$, thus the macro-stress becomes,

$$\boldsymbol{\sigma} = \frac{1}{V} \mathbb{Q} \pi \, . \tag{3.40}$$

The effective elastic modulus $\mathbb{E}^*$ relates stress to strain, in the discrete setting this relationship can be written

$$\Delta\boldsymbol{\sigma} = \mathbb{E}^* \Delta\boldsymbol{\varepsilon} \tag{3.41}$$

from equation (3.40), we can say,

$$\Delta\boldsymbol{\sigma} = \frac{1}{V} \mathbb{Q} \Delta\pi \tag{3.42}$$

Also,

$$\Delta\pi = [\mathbb{P}\tilde{\mathbf{K}}_{bb}^{-1}\mathbb{P}^T]\mathbb{Q}^T\Delta\boldsymbol{\varepsilon} \tag{3.43}$$

where,

$$\tilde{\mathbf{K}}_{bb} := \mathbf{K}_{bb} - \mathbf{K}_{ba}\mathbf{K}_{aa}^{-1}\mathbf{K}_{ab}\,. \tag{3.44}$$

So equation (3.41) becomes,

$$\Delta\boldsymbol{\sigma} = \underbrace{(\frac{1}{V}\mathbb{Q}[\mathbb{P}\tilde{\boldsymbol{K}}_{bb}^{-1}\mathbb{P}^T]^{-1}\mathbb{Q}^T)}_{\mathbb{E}^*}\Delta\boldsymbol{\varepsilon}\,. \tag{3.45}$$

The quantity $\mathbb{P}$ is the link topology matrix and $\mathbb{Q}$ is defined in equation (3.27).

It is important to notice that both the stress and the constitutive tensor are determined entirely from information at the boundary.

3.2.2 The penalty method

In Chapter 2 the following penalty term was derived,

$$\alpha_{LD}\int_{\partial V}|\boldsymbol{u} - \mathcal{E}\boldsymbol{x}|^2 dA\,. \tag{3.46}$$

In the finite element discretisation (using $\boldsymbol{u} = \boldsymbol{N}\boldsymbol{d}$ and $\boldsymbol{x} = \boldsymbol{N}\boldsymbol{x}$) including the standard terms in the integrand (i.e. $\frac{1}{2}\boldsymbol{d}^T\boldsymbol{K}\boldsymbol{d} - \boldsymbol{d}^T\boldsymbol{F}$) and minimising with respect to $\boldsymbol{d}$, the problem becomes,

$$\boldsymbol{K}\boldsymbol{d} - \boldsymbol{F} + \alpha_{LD}\int_{\partial V}\boldsymbol{N}^T\boldsymbol{N}\boldsymbol{d}\;\mathrm{dA} + \alpha_{LD}\int_{\partial V}\boldsymbol{N}^T\mathcal{E}\boldsymbol{N}\boldsymbol{x}\;\mathrm{dA} = 0 \tag{3.47}$$

or,

$$\tilde{\boldsymbol{K}}\boldsymbol{d} = \tilde{\boldsymbol{F}} \tag{3.48}$$

where,

$$\tilde{\boldsymbol{K}} = \boldsymbol{K} + \alpha_{LD} \int_{\partial V} \boldsymbol{N}^T \boldsymbol{N} \, \mathrm{dA} \tag{3.49}$$

and

$$\tilde{\boldsymbol{F}} = \boldsymbol{F} - \alpha_{LD} \int_{\partial V} \boldsymbol{N}^T \mathcal{E} \boldsymbol{N} \boldsymbol{x} \, \mathrm{dA} \, . \tag{3.50}$$

If $\boldsymbol{K}$, $\boldsymbol{d}$ and $\tilde{\boldsymbol{F}}$ are partitioned in a similar manner to that in Section 3.2.1, with N_b representing the number of nodes on the boundary, the sum,

$$\sum_{J=1}^{N_b} \frac{1}{2} \alpha_{LD} [\boldsymbol{d}^J + \mathcal{E} \boldsymbol{x}^J] \tag{3.51}$$

can be minimised to give,

$$\alpha_{LD} [\overline{\boldsymbol{d}} + \mathcal{E}] \overline{\boldsymbol{x}} \tag{3.52}$$

where $\overline{\boldsymbol{d}}$ and $\overline{\boldsymbol{x}}$ are vectors of boundary nodal quantities. Thus the problem becomes,

$$\boldsymbol{K}\boldsymbol{d} + \alpha_{LD} \overline{\boldsymbol{d}} = \underbrace{\boldsymbol{F} - \alpha_{LD} \mathcal{E} \overline{\boldsymbol{x}}}_{\tilde{\boldsymbol{F}}} \, . \tag{3.53}$$

The matrix problem to be solved in the linear problem is then,

$$\begin{bmatrix} \boldsymbol{K}_{aa} & \boldsymbol{K}_{ab} \\ \boldsymbol{K}_{ba} & \boldsymbol{K}_{bb} + \alpha_{LD}[\mathbf{I}] \end{bmatrix} \begin{Bmatrix} \boldsymbol{u}_a \\ \boldsymbol{u}_b \end{Bmatrix} = \begin{Bmatrix} \tilde{\boldsymbol{F}}_a \\ \tilde{\boldsymbol{F}}_b \end{Bmatrix} \, . \tag{3.54}$$

From the solution to the above problem the elastic modulus, can be extracted,

$$\mathbb{E}_{iAjB} = \frac{D\langle \boldsymbol{\sigma}_{iA} \rangle}{D\mathcal{E}_{jB}} = \quad \frac{\alpha_{LD}}{|V_0|} \left[\sum_{I=1}^{N_b} \left(\delta_{ij} \overline{x}_B^I - \sum_{J=1}^{N_b} \overline{K}_{ij}^{IJ} g_B^J \right) \overline{x}_A^I \right] \tag{3.55}$$

where $\overline{\boldsymbol{K}}$ is the inverse of the condensed boundary stiffness matrix, $\tilde{\boldsymbol{K}}_{bb} = \boldsymbol{K}_{bb} + \alpha_{LD}(\mathbf{I})$ and $\mathbf{g}^I = \alpha_{LD} \overline{\boldsymbol{x}}^I$.

To find the effective elastic modulus $\mathbb{E}^*_{ab}$, we use the 2D Voigt rule discussed in Chapter 2.

Again the tangent modulus has been extracted using only information from the boundary of the RVE.

3.2.3 Results of the investigation

Both methods were tested on the two-dimensional shapes shown in Figure 3.6. The

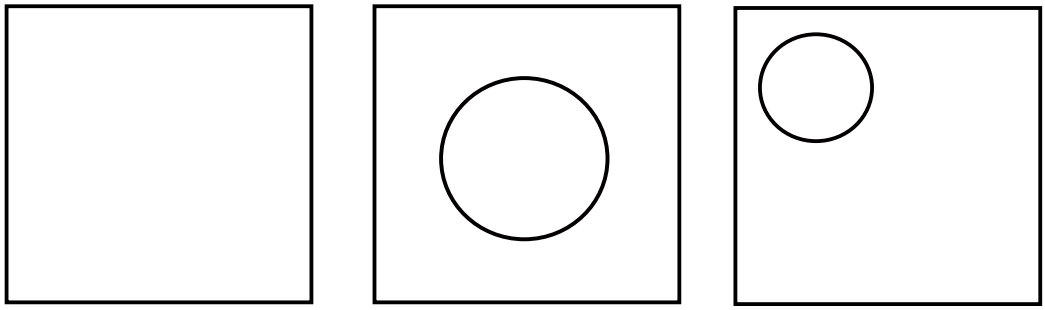

Fig. 3.6: Homogeneous square, square with central hole and square with eccentric hole used in investigation of boundary condition constraints

first test is an homogeneous square, the second a square with a central hole and the third a square with an eccentric hole. All were tested with extension and shear tests. In order for the lagrange multiplier and penalty methods to be validated the elasticity matrix calculated via the two methods needs to be equal to $\boldsymbol{D}$ in the case of the homogeneous square. In other words, as the material has no heterogeneities, the effective elastic modulus should be the same as that derived for an homogeneous, isotropic linear elastic material. The tensor $\boldsymbol{D}$ used in the investigation was,

$$\boldsymbol{D} = \begin{bmatrix} 16046.15 & 6876.92 & 0 \\ 6876.92 & 16046.15 & 0 \\ 0 & 0 & 4584.62 \end{bmatrix}.$$

Lagrange multiplier results

The value obtained for the elasticity matrix $\boldsymbol{D}^L$ via the lagrange multiplier method on the homogeneous square was,

$$\boldsymbol{D}^L = \begin{bmatrix} 16046.15 & 6876.92 & 0 \\ 6876.92 & 16046.15 & 0 \\ 0 & 0 & 4578.66 \end{bmatrix}.$$

This value is satisfactory and the method was seen as successful. The other concern in this investigation is that the displacement of the boundaries is periodic. Figures 3.7 (a) and (b) show the undeformed and deformed meshes and the x displacement for the shear test on the square with the central hole and Figures 3.7 (c) and (d) and show the same for the square with an eccentric hole in a simple extension test. An extra Dirichlet boundary condition is required to prevent a rigid body motion. The top right hand corner of the squares was fixed in order to maintain this. It can be seen that the boundary displacements are periodic, thus the method was successful.

Penalty method results

The value obtained for the new elasticity $\boldsymbol{D}^P$ via the penalty method on the homogeneous square was,

$$\boldsymbol{D}^P = \begin{bmatrix} 16041.30 & 6873.41 & 0 \\ 6873.41 & 16041.30 & 0 \\ 0 & 0 & 4583.95 \end{bmatrix}.$$

As the investigation was purely as an aid to understanding the implementation, the penalty term was a random large number, and was chosen as $12{\times}10^6$. As with the lagrange multiplier method the effective elastic modulus is sufficiently close to the linear displacement elasticity tensor to deem the method successful. Figure 3.8 shows the deformed and undeformed meshes for the homogeneous square in pure shear and the x-displacement for the same test. It can be seen in these figures that the displacement along the boundaries is linear.

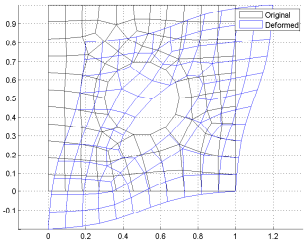

(a) Undeformed and deformed meshes for square with central void in pure shear

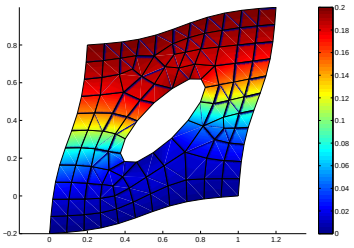

(b) x displacements for square with central void in pure shear

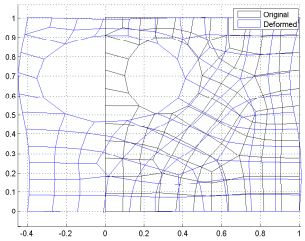

(c) Undeformed and deformed meshes for square with eccentric hole in simple extension

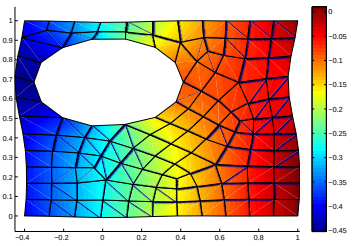

(d) x displacements for square with eccentric hole in simple extension

Fig. 3.7: Results using the lagrange multiplier method to enforce the periodic boundary constraint

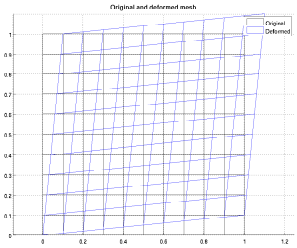

(a) Undeformed and deformed meshes for homogeneous square in pure shear

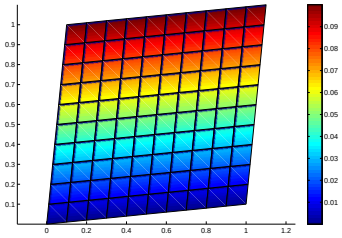

(b) x displacements for homogeneous square in pure shear

Fig. 3.8: Results using the penalty method to enforce the linear displacement boundary constraint

4

Testing methodology and implementation

The testing methodology utilised in this thesis closely follows that of Zohdi and Wriggers [31], which was used for the homogenisation of spherical inclusions in a matrix.

The geometrical detail of the microstructure was created using the programming language, Matlab [2] and the finite element analysis was implemented with the commercial finite element software, Abaqus [1] The process was automated via a script developed for the purpose of this thesis, this was written using the scripting language, Python [3].

4.1 Calculation of elastic moduli with the assumption of isotropy

As discussed in Chapter 2, the random nature of the fibres, which is due to the needle punching process used to entangle them, leads us to an assumption of macroscopic isotropy. The result of this is that we need only run one loading simulation, of either the linear displacement or constant traction loading situation, in order to calculate the effective bulk and shear moduli for the material, κ^* and μ^* respectively. The definitions of these quantities in terms of the average stresses and strains are reproduced here for convenience,

$$3\kappa^* := \frac{\langle \frac{1}{3}\mathrm{tr}\boldsymbol{\sigma}\rangle_\Omega}{\langle \frac{1}{3}\mathrm{tr}\boldsymbol{\varepsilon}\rangle_\Omega} \qquad \text{and} \qquad 2\mu^* := \sqrt{\frac{\langle \boldsymbol{\sigma}'\rangle_\Omega : \langle \boldsymbol{\sigma}'\rangle_\Omega}{\langle \boldsymbol{\varepsilon}'\rangle_\Omega : \langle \boldsymbol{\varepsilon}'\rangle_\Omega}} \tag{4.1}$$

where $(\cdot)'$ is the deviator and is defined as,

$$(\cdot)' = (\cdot) - \frac{1}{3}\mathrm{tr}(\cdot)\mathbf{I}\,.$$

For this thesis only the linear displacement boundary condition is considered. This will provide an upper bound for the constitutive tensor, as deduced in Section 2.5.

4.2 Optimal RVE sizing and sampling

A RVE should capture the nature of the underlying microstructure of the material in question. For an accurate approximation of $\mathbb{E}^*$ to the actual elastic modulus of the material it is required that the RVE be many orders of magnitude larger than the length scale of the heterogeneities (the fibres in this case). Figure 4.1 shows that the macro-domain should be far larger than the RVE, which, in turn, should be much larger than the heterogeneity in question. In other words, according to the dimensions labelled, $\mathbf{D} \gg \mathbf{L} \gg \mathbf{d}$. Practically, however, this is not possible, due to the high computational power required to execute such an analysis. Therefore the RVE size is limited and an analysis on one RVE will yield different results from that on another of the same size. As such it is necessary to use an average value obtained from the results from a large number of samples; this averaged value is denoted as $\tilde{\mathbb{E}}^*$.

The sizing of the RVEs is important; the larger a sample is, the more accurate the information gained from the test. However, a larger sample is also more computationally expensive, thus it is important to find an RVE size that is both statistically relevant and computationally feasible.

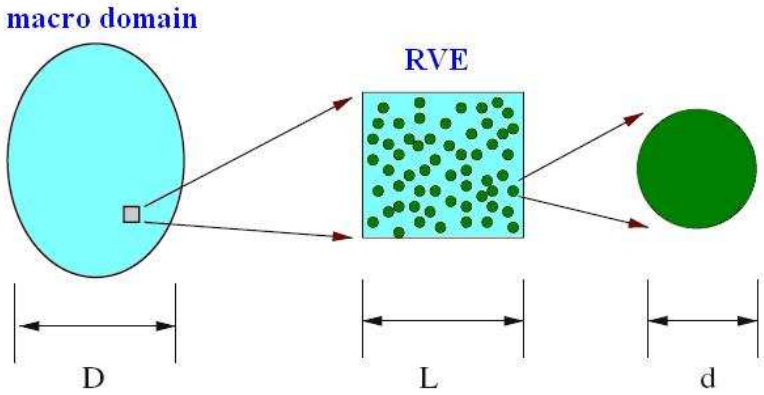

Fig. 4.1: The relationship between the dimensions of the macro-domain, the RVE and the heterogeneities [28]

4.2.1 Sizing the RVE

In order to settle on a final RVE size, the methodology is tested on a number of different sized samples. By inspecting a scanning electron microscope image of the material a general idea of relevant length scale is judged. This is used as an initial guess for the RVE size. As the size of the RVE is increased, so is the accuracy of the information in the results. As discussed in Chapter 2 the linear displacement loading condition will give properties that bound the the actual values from above. As the size of the RVE is increased, the effective values will vary until they reach a best approximation within a tolerance (which is still higher than the actual value). Thus samples of increasing size are tested until a satisfactory value is reached. This process is illustrated in Figure 4.2.

4.3 Partitioning the domain

Bounds on the effective constitutive properties are discussed in Section 2.5. To make use of these bounds a large domain is partitioned into $5^3 = 125$ small domains. These 125 samples provide the statistical data to be analysed while also mimicking the geometry of one continuous large domain.

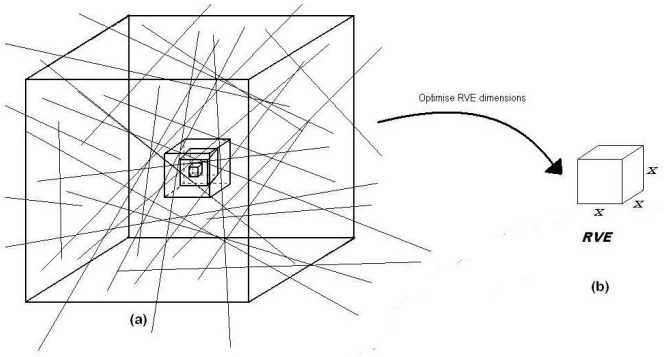

Fig. 4.2: The procedure used to size the RVE. A small sample is used and the size is increased until the results become satisfactory

4.4 Approximation to microstructure

In the actual material the fibres are of varying length and diameter, of average 62mm and 30μm respectively. There is a 50% variation in the diameters of the fibres along their length as a result of their natural origin. Due to the nature of the needle-punching process the fibres are orientated completely randomly within the matrix. The volume fraction of the fibres in the matrix is approximately 30%.

While the actual material is manufactured as thin, flat plates, here the material is modelled as a three-dimensional cube as an initial step towards a full, 3-D, nonlinear multi-scale analysis. The large domain is partitioned into 125 subdomains to be analysed separately. Both the polymer matrix and the fibres are assumed to be linear elastic. The fibres (flax in this case) and the polypropylene matrix have elastic moduli

of 27.6GPa and 1.35GPa respectively. It is notable that the fibres are approximately 20 times "stiffer" than the matrix, making it an effective pairing for a composite. The matrix has a Poisson's ratio, shear modulus and bulk modulus of 0.35, 0.49GPa and 1.607GPa respectively. The properties for the fibres and the matrix were obtained via tests conducted at the CSIR, Port Elizabeth. Figure 4.3 shows a SEM image of the fibres after they have been needlpunched and bonded into the matrix.

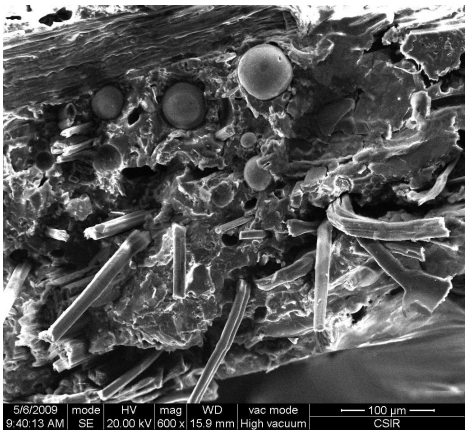

Fig. 4.3: Scanning electron microscope image of material after bonding (Image courtesy of CSIR, Port Elizabeth)

In the initial model the fibres are simply modelled as straight cylinders of different lengths dispersed randomly within the matrix. The cross sectional area of the fibres is modelled as uniform along the length of the cylinder, at 30μm. The bending stiffness of the fibres is assumed to be negligible.

4.5 Generation of randomly orientated fibres

The geometrical structure of the individual RVEs is created via an algorithm written in Matlab. As there is no accommodation for fibres at the boundary (i.e. those exiting or entering the domain) there is no need to have any fibres originating/terminating inside the domain. Thus all fibres are assigned twice the length of the diagonal of the

large domain l_d, so that all fibres effectively start and end on the domain boundary. This large domain is then partitioned into 125 subdomains as detailed in Section 4.3.

The planes forming the bounding box of the large domain are each defined by three points. The midpoint to a fibre $\mathbf{M} = (n \quad p \quad q) \in \Omega$, is chosen randomly within that bounding box.

A fibre is then defined by a vector $\mathbf{R} = \mathbf{X}_b - \mathbf{X}_a$, which centres on $\mathbf{M}$. The distances $\mathbf{M} - \mathbf{X}_a$ and $\mathbf{M} - \mathbf{X}_b$ are equal to $2l_d$. This is shown in Figure 4.4.

The intersection points with the boundaries of the domain, $\mathbf{X}_1$ and $\mathbf{X}_2$, are calculated and recorded as the new endpoints of the lines (i.e. the fibres are truncated at the domain boundary as information outside the domain is irrelevant). The volume fraction is calculated and, until the desired 30% volume fraction is reached, fibres are added one by one to the domain in the same way. It is not important to have a tolerance on the volume fraction as the thinness of the fibres (30μm) means that the increase in volume as a result of a single extra fibre is a negligible addition to the desired volume fraction. The intersection points of the fibres with the boundary are written to a file.

The information for the large domain is now complete. To avoid the added computational labour of Abaqus partitioning the large domain, the partitioning is simulated within the Matlab code. Similarly the planes bounding the subdomains are defined. For every subdomain all the fibres stored from the previous step are looped through to check whether or not they instersect the boundaries of the current subdomain. For each subdomain the intersection points of any fibre entering it with the subdomain boundary are stored in a separate file. Thus for every subdomain the fibre geometry is stored separately.

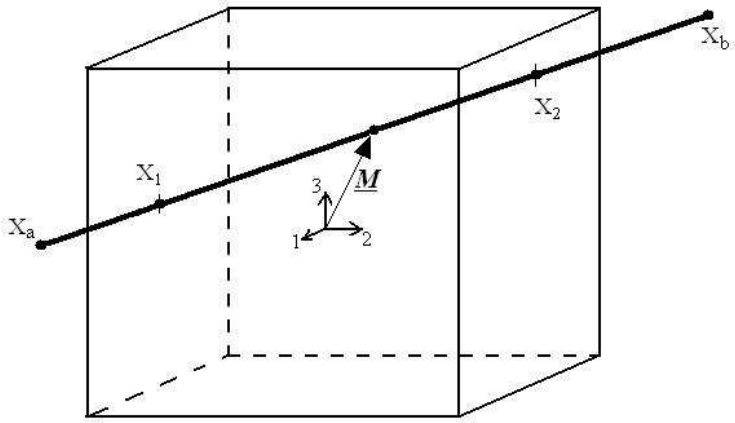

Fig. 4.4: Random fibre generation

4.6 Finite element implementation

The creation of the models is automated using a Python script developed for the problem. The fibre geometries are read and transferred into the geometry of the subdomains. 125 input decks are created and sent to Abaqus where the finite element analyses are performed.

4.6.1 Modelling the material

The matrix is assigned a three-dimensional solid section and each of the fibres a truss section (owing to the low bending stiffness). The fibres are embedded into the matrix using the embedded element constraint in Abaqus. This feature adds the volume of the fibre to the total volume of the surrounding matrix. Thus the final model has a total volume of $V_{\text{fibre}} + V_{\text{matrix}}$. As a result of this, this constraint is only suitable for relatively low fibre volume fractions. One of the advantages of this constraint is that it allows the fibres to be meshed separately from the matrix, thus the discretisation of the matrix can be regular. This regular mesh is desirable as more control over the element shape is achieved and far fewer degrees of freedom result than from an irregular mesh. Hexahedral elements (an eight noded brick) are used to mesh the matrix and truss elements for the fibres.

The strain field, including both volumetric and dilatational components was applied directly to the domain according to the linear displacemnt boundary condition.

The diameter, and therefore the cross-sectional area, of the fibres is very small in comparison to the size of the RVE. Therefore it is important to have a mesh fine enough to capture the effects of the fibres within the matrix but coarse enough to remain computationally viable. A single meshed subdomain is shown with the fibres visible in Figure 4.5(a) and with only the endpoints of fibres visible in Figure 4.5(b).

4.6.2 Postprocessing of results

The aim of the procedure is to obtain an effective macroscopic elastic modulus for the microscopically heterogeneous material. The bulk and shear moduli are defined in equation (4.1).

Both definitions require volume averages of the stresses and strains found in the analysis. The stress volume average for a subdomain K is defined as follows:

$$\langle \boldsymbol{\sigma} \rangle_{\Omega_K} = \frac{1}{V_K} \int_{\Omega_K} \boldsymbol{\sigma} \, \mathrm{dV} \quad = \quad \frac{1}{V_K} \Bigg(\underbrace{\int_{\Omega_m} \boldsymbol{\sigma} \, \mathrm{dV}}_{\text{matrix contribution}} + \underbrace{\int_{\Omega_f} \boldsymbol{\sigma} \, \mathrm{dV}}_{\text{fibre contribution}} \Bigg) \tag{4.2}$$

The embedded element constraint in Abaqus, which is used to define the relationship between the fibres and the matrix, adds the volume of the fibres to the volume of the matrix, thus the overlapping volumes are duplicated. As a result of this, the above equation becomes:

$$\langle \boldsymbol{\sigma} \rangle = \frac{1}{V_K + V_f} \Bigg(\int_{\Omega_K} \boldsymbol{\sigma} \, \mathrm{dV} + \int_{\Omega_f} \boldsymbol{\sigma} \, \mathrm{dV} \Bigg) \tag{4.3}$$

The same principle applies for the strain, which becomes,

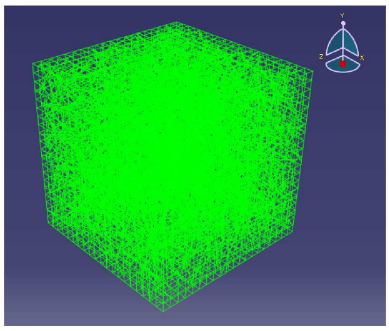

(a) Finite element mesh on subdomain with fibres visible

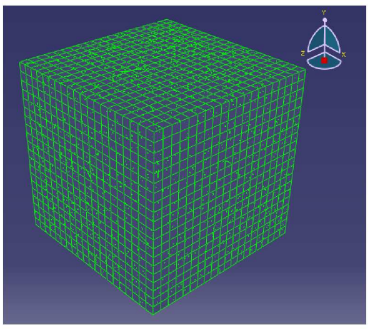

(b) Finite element mesh on subdomain with fibres hidden

Fig. 4.5: The finite element mesh for the RVE

$$\langle \boldsymbol{\varepsilon} \rangle = \frac{1}{V_K + V_f} \left(\int_{\Omega_K} \boldsymbol{\varepsilon} \ \mathrm{dV} + \int_{\Omega_f} \boldsymbol{\varepsilon} \mathrm{dV} \right) \tag{4.4}$$

Note that the integral of the stress over the domain can also be expressed as a boundary integral, in the same manner as in section 3.2.1, by using the divergence theorem to get

$$\int_{\Omega} \sigma_{ij} \ \mathrm{dV} = \frac{1}{2} \int_{\partial\Omega} (t_i x_j + t_j x_i) \ \mathrm{dA} \tag{4.5}$$

which can be written, in Voigt notation, as

$$\int_{\Omega} \boldsymbol{\sigma} \ \mathrm{dV} = \int_{\partial\Omega} \underbrace{\begin{bmatrix} x_1 & 0 & 0 \\ 0 & x_2 & 0 \\ 0 & 0 & x_3 \\ \frac{1}{2}x_2 & \frac{1}{2}x_1 & 0 \\ \frac{1}{2}x_3 & 0 & \frac{1}{2}x_1 \\ 0 & \frac{1}{2}x_3 & \frac{1}{2}x_2 \end{bmatrix}}_{\overline{\boldsymbol{X}}} \underbrace{\begin{bmatrix} t_1 \\ t_2 \\ t_3 \end{bmatrix}}_{\boldsymbol{t}} \ \mathrm{dA} \,. \tag{4.6}$$

Now, $\boldsymbol{t} = \boldsymbol{\sigma n}$ can be expressed as

$$\boldsymbol{t} = \underbrace{\begin{bmatrix} n_x & 0 & 0 & n_y & n_z & 0 \\ 0 & n_y & 0 & n_x & 0 & n_z \\ 0 & 0 & n_z & 0 & n_x & n_y \end{bmatrix}}_{\overline{\boldsymbol{n}}} \begin{bmatrix} \sigma_x \\ \sigma_y \\ \sigma_z \\ \sigma_{xy} \\ \sigma_{xz} \\ \sigma_{yz} \end{bmatrix} . \tag{4.7}$$

Thus $\boldsymbol{t} = \overline{\boldsymbol{n}}\boldsymbol{\sigma}$. Now, we can substitute $\boldsymbol{\sigma} = \boldsymbol{BDd}$ to obtain $\boldsymbol{t} = \overline{\boldsymbol{n}}\boldsymbol{BDd}$. Equation 4.6 can then be written as

$$\int_{\Omega} \boldsymbol{\sigma} \ \mathrm{dV} = \int_{\partial\Omega} \overline{\boldsymbol{X}}\boldsymbol{t} \ \mathrm{dA} = \int_{\partial\Omega} \overline{\boldsymbol{X}}\overline{\boldsymbol{n}}\boldsymbol{BDd} \ \mathrm{dA} \tag{4.8}$$

or

$$\int_{\Omega} \boldsymbol{\sigma} \, \mathrm{dV} = \overline{\boldsymbol{Z}}\boldsymbol{d} \tag{4.9}$$

$$\text{where} \qquad \overline{\boldsymbol{Z}} = \int_{\partial\Omega} \overline{\boldsymbol{X}}\overline{\boldsymbol{n}}\boldsymbol{B}\boldsymbol{D} \, \mathrm{dA}\,. \tag{4.10}$$

The preceding approach was not used in this thesis as only test problems were solved and, as such, the simulations were not large enough for it to be beneficial.

In order to effectively add the contribution of the fibres to that of the matrix it is important to note that, due to the definition of the fibres as truss elements, they only have one stress component, σ_{11}. As they are orientated randomly the coordinate system of the fibres must be transformed to that of the subdomain. The coordinate transformation is performed in the following way:

If $\mathbf{e}_i$ represents the coordinate system of the subdomain, and $\mathbf{e}'_i$ that of the fibre in question (as shown in Figure 4.6), the derivation of the resolved stress is as follows:

$$\sigma_{ij} = \mathbf{e}_i \cdot \boldsymbol{\sigma}\mathbf{e}_j \tag{4.11}$$

$$= \mathbf{e}_i \cdot [\sigma'_{11}\mathbf{e}'_1 \otimes \mathbf{e}'_1]\mathbf{e}_j \tag{4.12}$$

$$= \sigma'_{11}(\mathbf{e}'_1 \cdot \mathbf{e}_j)(\mathbf{e}'_1 \cdot \mathbf{e}_i) \tag{4.13}$$

The transformed fibre stress components are shown in Table 4.1

Table 4.1: Transformed fibre stresses

σ_{11}	$\sigma'_{11}(\mathbf{e}'_1 \cdot \mathbf{e}_1)^2$
σ_{22}	$\sigma'_{11}(\mathbf{e}'_1 \cdot \mathbf{e}_2)^2$
σ_{33}	$\sigma'_{11}(\mathbf{e}'_1 \cdot \mathbf{e}_3)^2$
σ_{12}	$\sigma'_{11}(\mathbf{e}'_1 \cdot \mathbf{e}_2)(\mathbf{e}'_1 \cdot \mathbf{e}_1)$
σ_{13}	$\sigma'_{11}(\mathbf{e}'_1 \cdot \mathbf{e}_3)(\mathbf{e}'_1 \cdot \mathbf{e}_1)$
σ_{23}	$\sigma'_{11}(\mathbf{e}'_1 \cdot \mathbf{e}_3)(\mathbf{e}'_1 \cdot \mathbf{e}_2)$

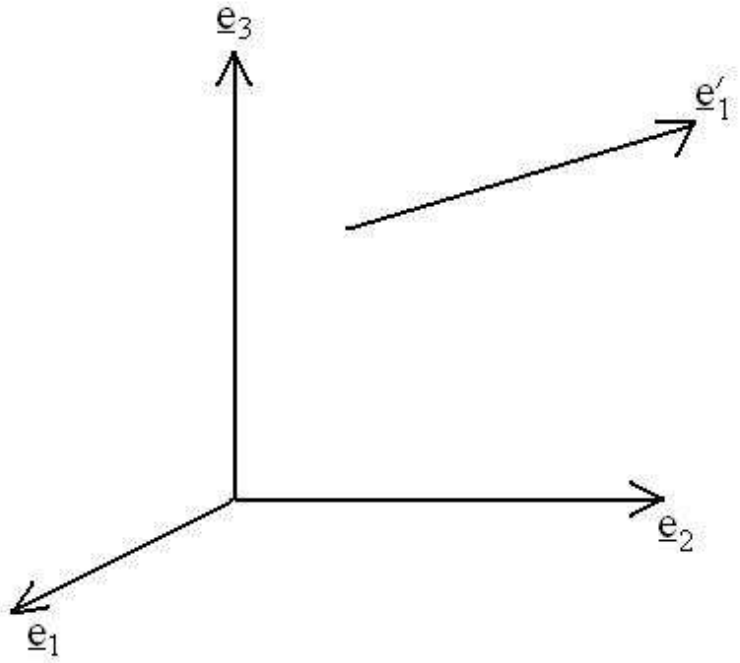

Fig. 4.6: Resolving stress components

4.6.3 Expected distribution of data

Statistical data gathered from a number of tests on same-sized samples with different arrangements of fibres gives an array of material property values which may be used to find an averaged, effective elastic modulus, denoted as $\tilde{\mathbb{E}}^*$.

The distribution of data found from the analysis of many samples can be analysed using basic statistical analysis, for example investigations into the mean and standard deviations. It is also useful to have a way of bounding the results, for example by using the classical Reuss and Voigt bounds, derived in Section 2.4.

Calculating the Reuss and Voigt bounds

The Voigt bound is simply the average value for the elastic modulus over the domain according to the volumetric mixture of matrix and fibres,

$$E_{Voigt} = \frac{1}{V_{total}} \left(\int_{\Omega} E_m \, \mathrm{d}\Omega + \int_{\Omega} E_f \, \mathrm{d}\Omega \right) \tag{4.14}$$

where E_m and E_f describe the elastic moduli of the matrix and fibres respectively. Also, $V_{total} = V_\Omega + V_f$, that is, the total volume is the sum of the volume of the matrix and the fibres, giving a total volume greater than 100%. This is due to the embedded element constraint superimposing the volumes of the fibres onto the matrix. As the elastic moduli for both the matrix and fibre are constant, equation (4.14) becomes,

$$E_{Voigt} = \frac{(E_m V_m + E_f V_f)}{V_{total}} \, . \tag{4.15}$$

The Reuss bound, by the same logic, is then,

$$E_{Reuss} = \frac{V_{total}}{(E_m^{-1} V_m + E_f^{-1} V_f)} \, . \tag{4.16}$$

For the material in question, with elastic moduli of $E_m = 1350\text{MPa}$ and $E_f = 27,600\text{MPa}$ and volume fractions of $V_m = 100\%$ and $V_f = 30\%$, we obtain,

$$E_{Voigt} = 7407.69\text{MPa} \tag{4.17}$$

$$E_{Reuss} = 1729.62\text{MPa} \, . \tag{4.18}$$

$$\tag{4.19}$$

Thus we have theoretical upper and lower bounds on the computational results.

5

Results

While the material being investigated contained a fibre volume fraction of 30%, a number of different models containing varying volume fractions below this value were also analysed in order to investigate the existence of a trend. The model containing 30% volume fraction was tested at different RVE sizes so as to verify that the final RVE size chosen was valid. Each model was run for two separate fibre generation procedures in order to ensure that the process gave similar results for different fibre assemblies.

5.1 Sizing the RVE

The methodology described in Chapter 4 was implemented on a number of samples of varying sizes. The initial RVE size for the individual subdomains (which are referred to as RVEs) was estimated by inspection of the scanning electron microscope image shown in Figure 5.1. The characteristic dimension for a cube initially guessed to effectively represent the microstructure was 2mm. This meant that the domain to be partitioned into $5^3 = 125$ subdomains, and which is referred to as the macro-RVE, had a side length of 1cm. The results for $\tilde{\kappa}^*$ and $\tilde{\mu}^*$ were found using the average stresses and strains, as discussed in Section 4.6.2 and using equation (2.52), where the value $\tilde{\varphi}^*$ (where φ represents the property in question) is the average effective value of the property, that is, the mean of the effective values found for the subdomains. The effective values for elastic modulus and Poisson's ratio were then calculated using the relationships

$$\kappa = \frac{E}{3(1-2\nu)} \qquad \text{and} \qquad \mu = \frac{E}{2(1+\nu)}, \tag{5.1}$$

to obtain

$$E = \frac{9\kappa\mu}{3\kappa+\mu} \qquad \text{and} \qquad \nu = \frac{3\kappa-2\mu}{2(3\kappa+\mu)}\,. \tag{5.2}$$

As the simulation for the 1cm macro-RVE proved to be computationally taxing, it

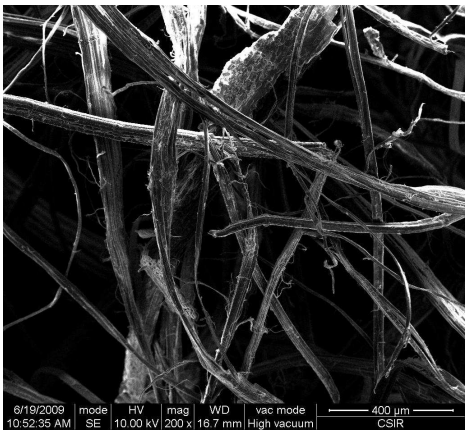

Fig. 5.1: Scanning electron microscope image used in initial guess for sizing RVE

was decided that this would be the maximum RVE size tested. A series of smaller samples were tested to verify that this large sample was, in fact, viable as a macro-RVE. The other macro-RVE samples tested had characteristic dimensions of 0.125cm, 0.25cm, 0.5cm and 0.75cm.

5.2 Simulations involving varying macro-RVE sizes

The results for these investigations are shown in Table 5.1 (the values designated "(r)" are for the repeated model generations). The values for the effective elastic moduli lie between the Reuss and Voigt bounds as shown in Table 5.2. Histograms showing the distributions of the results for each size macro-RVE are shown in Figures 5.2 through 5.6. These histograms correspond to the tests designated "(r)" in Table 5.1. Table

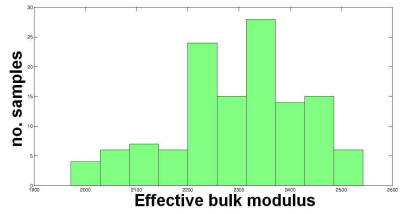

(a) κ^* - mean = 2294.70MPa, (standard deviation/mean) = 5.56%

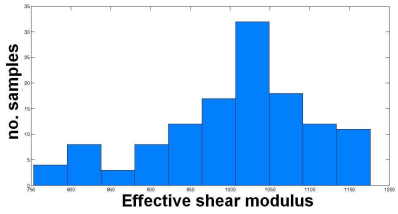

(b) μ^* - mean = 1006.37MPa, (standard deviation/mean) = 9.63%

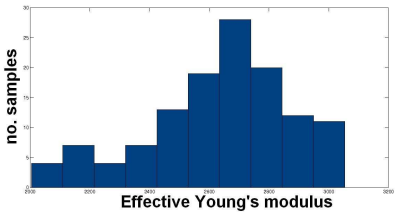

(c) E^* - mean = 2633.40MPa, (standard deviation/mean) = 9.11%

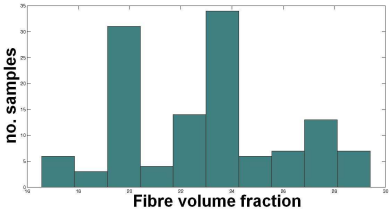

(d) Volume fraction - Standard deviation in 30% = 3.11

Fig. 5.2: Effective material properties for 1cm macro-RVE

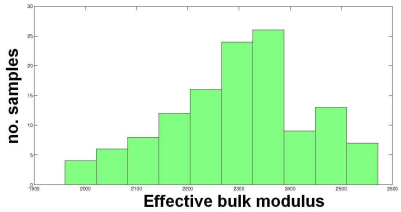

(a) κ^* - mean = 2298.74MPa, (standard deviation/mean) = 5.90%

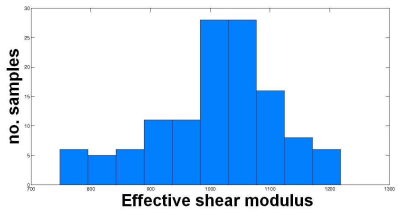

(b) μ^* - mean = 1009.12MPa, (standard deviation/mean) = 10.19%

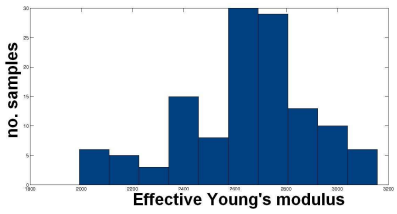

(c) E^* - mean = 2640.22MPa, (standard deviation/mean) = 9.64%

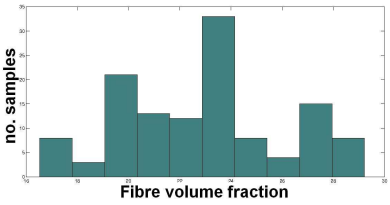

(d) Volume fraction - Standard deviation in 30% = 3.22

Fig. 5.3: Effective properties for 0.75cm macro-RVE

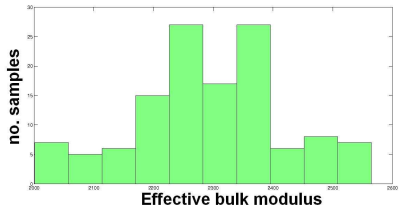

(a) κ^* - mean = 2294.21MPa, (standard deviation/mean) = 5.77%

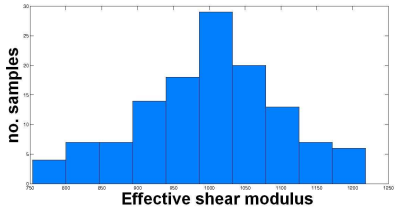

(b) μ^* - mean = 999.86MPa, (standard deviation/mean) = 10.15%

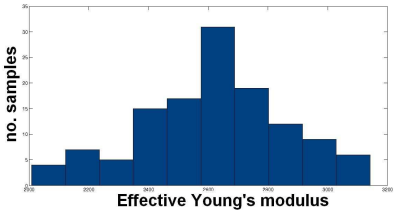

(c) E^* - mean = 2618.34MPa, (standard deviation/mean) = 9.57%

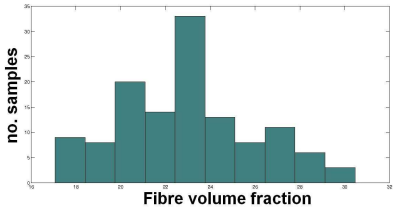

(d) Volume fraction - Standard deviation in 30% = 3.20

Fig. 5.4: Effective properties for 0.5cm macro-RVE

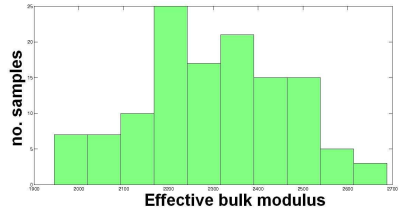

(a) κ^* - mean = 2296.13MPa, (standard deviation/mean) = 6.95%

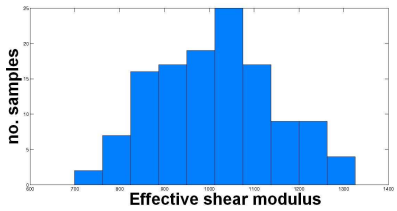

(b) μ^* - mean = 1015.37MPa, (standard deviation/mean) = 13.21%

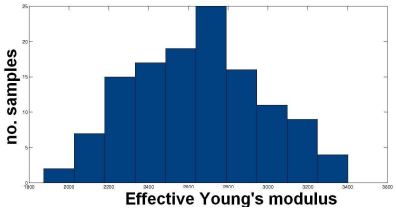

(c) E^* - mean = 2653.47MPa, (standard deviation/mean) = 12.32%

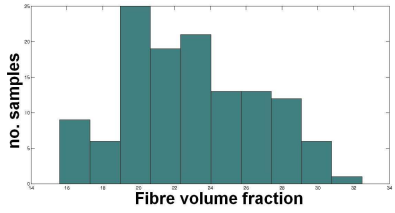

(d) Volume fraction - Standard deviation in 30% = 3.67

Fig. 5.5: Effective properties for 0.25cm macro-RVE

Table 5.1: Results for RVEs of varying sizes

macro-RVE size	$\tilde{\kappa}^*$	$\tilde{\mu}^*$	$\tilde{E}^*$	$\tilde{\nu}^*$
0.125cm	2282.06	1012.15	2662.33	0.31
0.125cm (r)	2327.83	1088.85	2821.36	0.31
0.25cm	2300.27	1015.38	2653.70	0.31
0.25cm (r)	2296.13	1015.37	2653.47	0.31
0.5cm	2293.91	1012.57	2647.24	0.31
0.5cm (r)	2294.21	999.86	2618.34	0.31
0.75cm	2294.63	1004.24	2628.46	0.31
0.75cm (r)	2298.74	1009.12	2640.22	0.31
1cm	2286.33	976.36	2563.82	0.31
1cm (r)	2294.70	1006.37	2633.40	0.31

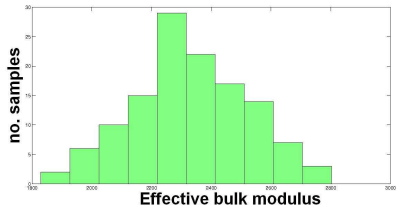

(a) κ^* - mean = 2327.83MPa, (standard deviation/mean) = 8.48%

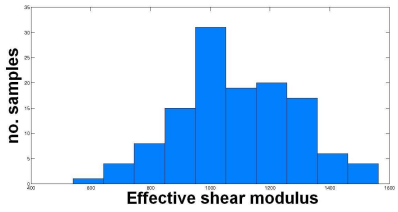

(b) μ^* - mean = 1088.85MPa, (standard deviation/mean) = 18.44%

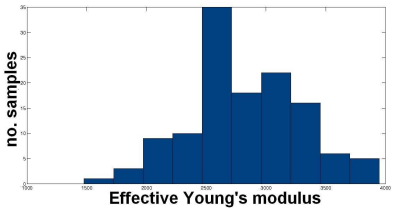

(c) E^* - mean = 2821.36MPa, (standard deviation/mean) = 17.01%

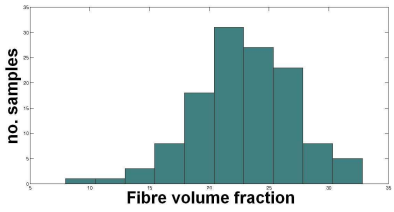

(d) Volume fraction - Standard deviation in 30% = 4.27

Fig. 5.6: Effective material properties for 0.125cm macro-RVE

5.3 shows the ratio of standard deviation to the mean for the results shown in these histograms.

Table 5.2: Results for RVEs of varying volume fraction

Vol frac	E_{Reuss} (MPa)	$\tilde{E}^*$ (MPa)	E_{Voigt} (MPa)
5%	1414.04	1566.33	2600.00
10%	1477.77	1787.66	3736.36
15%	1541.19	1990.73	4773.91
20%	1604.31	2205.02	5725.00
30%	1729.62	2633.40	7407.69

Table 5.3: Ratio of standard deviation to mean values

macro-RVE size	$\tilde{\kappa}^*$	$\tilde{\mu}^*$	$\tilde{E}^*$
0.125cm	8.48%	18.44%	17.01%
0.25cm	6.95%	13.21%	12.32%
0.5cm	5.77%	10.15%	9.57%
0.75cm	5.90%	10.19%	9.64%
1cm	5.56%	9.63%	9.11%

5.3 Simulations involving varying fibre volume fractions

The average results for the simulations using fibre volume fractions varying between 5% and 30% are tabulated and graphed in Table 5.4 and Figure 5.7. As expected, the elastic material properties become stronger for increasing fibre volume fractions. This is shown in Figures 5.7(a) through 5.7(c). Here, the values for the matrix and the Young's modulus value for the fibres are the given values, as opposed to results from numerical models.

5.3.1 Summary of results for final 30% volume fraction model

The final model was taken to be the largest macro-RVE tested (that is, the 1cm domain), which was also the most expensive computationally. To fill the macro-RVE to 30% with fibres of diameter 30μm required the generation of 47 673 and 47 721 fibres respectively for the first and second simulations. The results for the elastic modulus for these investigations were 2563.82MPa and 2633.40MPa for the first and second job respectively. The realationship between these values and the Reuss and Voigt bounds

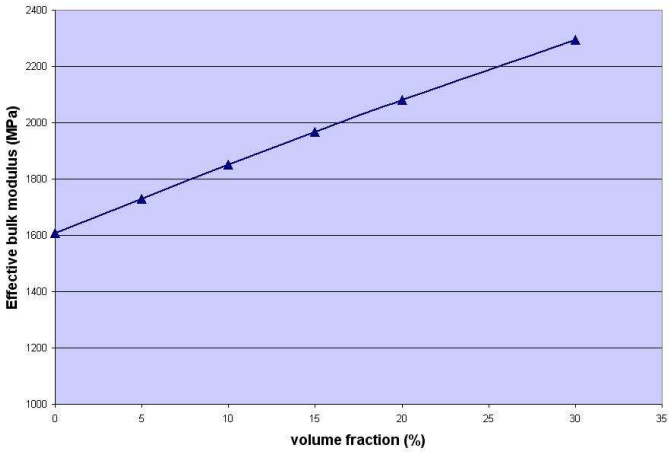

(a) Bulk modulus vs fibre volume fraction

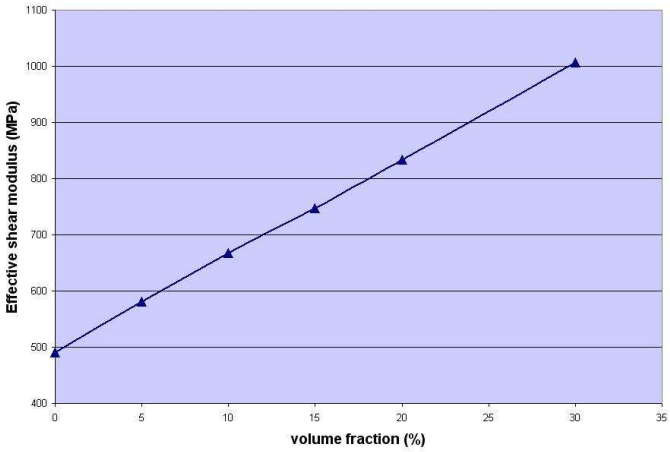

(b) Shear modulus vs fibre volume fraction

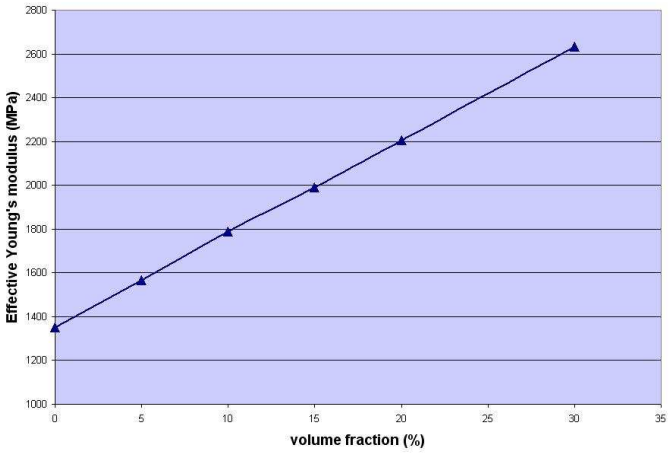

(c) Young's modulus vs fibre volume fraction

Fig. 5.7: Effective properties with increasing fibre volume fraction

Table 5.4: Results for RVEs of varying volume fraction

Vol frac	$\tilde{\kappa}^*$	$\tilde{\mu}^*$	$\tilde{E}^*$	$\tilde{\nu}^*$
Matrix	**1607**	**490**	**1350**	**0.36**
5%	1732.59	580.90	1567.49	0.35
5% (r)	1730.81	580.50	1566.33	0.35
10%	1851.22	667.57	1787.66	0.34
10% (r)	1851.82	667.57	1787.66	0.34
15%	1968.90	751.54	1999.90	0.33
15% (r)	1966.26	747.78	1990.73	0.33
20%	2081.38	838.16	2216.58	0.32
20% (r)	2079.87	833.31	2205.02	0.32
30%	2286.33	976.30	2563.82	0.31
30% (r)	2294.70	1006.37	2633.40	0.31
Fibre			**27, 600**	

is shown in Table 5.2. The other properties found from these two analyses are shown in Tables 5.1 and 5.4.

5.4 Discussion

The results are adequately bounded by the Reuss and Voigt bounds in all examples. Also, the material becomes stronger in its material properties with increasing volume fractions. For example, looking at the effective Young's modulus, the composite material with a fibre volume fraction of 30% is approximately twice as stiff as the matrix material.

The actual bulk and shear moduli and Poisson's ratio values for the fibre have not been indicated in Table 5.4 as these values do not show a valid comparison with the composite. This is because the fibres have been modelled as trusses and thus are allocated none of these moduli (that is, they are only given a Young's modulus). The effect of modelling the fibres this way is that there can be no transfer of transverse loading between the matrix and the fibre elements. Thus the fibres are only acting

in uniaxial tension or compression and the stresses in them must be resolved into the matrix coordinate system, as detailed in Section 4.6.2. As the fibres are allocated a Young's modulus in the actual finite element model, this comparison between the composite and the fibres is still relevant.

All of the histograms have relatively smooth distibutions, although the standard deviation varies considerably between the different RVE sizes. Part of the deviation is due to the variation of fibre volume fractions among the RVEs in each macro-RVE. It is also notable that with increasing domain size, the standard deviation decreases, thereby giving a smaller range of data, while the mean value over all samples remains similar. Thus the data from one individual RVE in a large macro-RVE is statistically more likely to be accurate than that from a smaller one. The standard deviation for all properties is less than 10% for the 1cm macro-RVE. This is seen as an acceptable variation in results. The smaller macro-RVEs have standard deviations for the effective shear and elastic moduli approaching 20%. Clearly the data for the larger RVE is considerably more accurate.

The comparisons of effective values as a function of fibre volume fractions (Figures 5.7(a). 5.7(b), 5.7(c)) show a credible trend between the matrix and composite values. It should be noted that the proportion of fibres to total volume of the composite is not effectively 30% due to the manner in which the fibres were treated within the matrix, that is, using the embedded fibre constraint in Abaqus. Due to the superpositioning of the fibres in the matrix, the volume of matrix is in fact still 100%, thus the fibre volume fraction is effectively $\frac{V_f}{1+V_f}$, where V_f represents the fibre volume fraction. However, the models in this thesis give the effect of adding 30% of the original volume in fibres to the matrix.

All of the numerical data lies satisfactorily within the Reuss and Voigt bounds and shows strengthening behaviour as a result of increasing the fibre volume fraction.

6

Conclusions and recommendations

In this thesis a multi-scale methodology has been implemented. The approach is suited specifically to the modelling of a natural-fibre reinforced composite for use in a laminated structure to be incorporated into aeroplane interior componentry. Both the matrix and fibre components are linear elastic and, as such, the model is linear elastic, thus there need be no iteration between the micro- and macrodomains. The fibre reinforcements within the matrix are completely random, as a result of the manufacturing process utilised. As a result of this the material is seen to be macroscopically isotropic, an assumption which further simplifies the analysis. The representative volume element used in the thesis is generated in as efficient a way as possible within the context and is the largest viable within the computational limits of the project.

While the results were within the theoretical bounds, these bounds are far apart, therefore and in light of the above, the following recommendations for future work are given. It should be noted, however, that many of these extensions, particularly some of those in Sections 6.2 and 6.3, would lead to higher computational demand, thereby possibly requiring simplifications in other areas of the model or the use of a cluster/multi-processor.

6.1 Further tests

Different methodologies can be tested with little alteration to the current model. Any further tests are useful in the validation of the current model.

6.1.1 Standard laboratory tests

A number of further tests can be run in order to verify the results of this investigation. Standard laboratory tests should be simulated in a computational environment, such as a standard extension test, a bulk test and a shear test. These tests, if showing large discrepancies from the results in Chapter 5 would aid in the understanding of where the greatest inaccuracy may be generated in the methodology of this thesis. If the results were satisfactory by comparison with those in Chapter 5, this would validate the methodology used, and further investigation pertaining to the geometry of the material (that is the assumptions made in approximating it) could be carried out. The final advantage of these tests is that they would exactly mimic those carried out experimentally, allowing for a direct comparison with the industrial results.

6.1.2 Investigating an anisotropic material

The material in question is assumed to be macroscopically isotropic in this thesis. According to the method followed (similar to that of Zohdi and Wriggers [31]) this assumption allowed the RVE to be tested with only one loading condition. Were the material not, in fact, isotropic it would be necessary to supplement these tests with five additional loading cases (with the linear displacement boundary condition). This would be an interesting exercise for verifying the results found in Chapter 5.

It would also be useful to create the geometry of the material as anisotropic. The extreme case, which would be most illustrative of the value of such an exercise would be that in which all the fibres within the matrix were aligned. The results from such an experiment would provide further bounds to the results in this thesis. Different levels of alignment of the fibres (for example one third in each direction) could show trends as a state of complete randomness is approached.

6.2 Improvements in approximation to material structure

The model in this thesis is meant as an initial step to the accurate modelling of a fibre reinforced composite material. As such, various design features of the material were simplified. There exist various extensions to the modelling of the material within the current methodology which can be implemented.

6.2.1 Fibre geometry and modelling

The fibres are modelled in this thesis as straight cylinders with negligible bending stiffness. The fibres in the actual material are highly curved and irregular in cross-section along their length.

The fibres are modelled using truss elements in this thesis so only the Young's modulus is used. This renders a comparison between fibre and composite values for the other moduli irrelevant, thus modelling the fibres as truss elements is a limitation on the model. Modelling the fibres with one-dimensional rods, or curved beam elements allows them stiffness in bending as well as torsion without being as computationally expensive as three-dimensional elements.

While the ruggedness of the natural fibres would be difficult to mimic, steps towards better approximation of the fibres can be taken by varying the cross sectional area along their length.

In the randomisation algorithm used, the fibres could be modelled as higher order polynomials or, probably most fittingly, as splines. If the bending stiffness of the fibres were now taken into account the effects of the "straightening out" of the fibres under load may be seen.

6.2.2 Embedding the fibres

The embedded element constraint in Abaqus is used in this thesis. This method is valid for low volume fractions but, due the superpositioning of the components according to this constraint, may not be accurate for higher volume fractions. The alternative

to this is to create voids where the fibres are in the matrix and fill them with the fibres. Contact constraints can then be defined between the two components allowing for a more accurate model which can be extended to higher volume fractions.

A further advantage of this technique is that the debonding process can be investigated. At present, perfect bonding is assumed between the matrix and fibres, but debonding could be an important feature of a damage model and it may be paramount in the design of this material.

6.3 Material components and geometric nonlinearity

The matrix and fibres have been assumed to be linear elastic. It may be useful to further investigate these components so as to include any nonlinear effects into the material. This or an extension of the model to a finite strain context would make it necessary for the process to be fully iterative. Thus the methodology used in this thesis could not be used (that is, analysing only the microstructure). The extension of this model to a fully iterative, nonlinear analysis would make it extendable to the wide range of other applications of the multiscale analysis technique consisting of random fibre reinforced composite arrangements.

References

[1] *ABAQUS/Standard, ABAQUS analysis user's manual, Version 6.8 RI: ABAQUS Inc.; 2009.*

[2] *http://www.mathworks.com.*

[3] *http://www.python.org/.*

[4] V. Belsky, M.W. Beall, J. Fish, M.S. Shephard, and S. Gomaa. Computer-aided mutliscale modelling tools for composites materials and structures. *Computing Systems in Engineering*, 6(3):213–223, 1995.

[5] T. Belytchko and J. Fish. *A First Course in Finite Elements.* Wiley, New York, 2007.

[6] F. Feyel. Multiscale FE^2 elastoviscoplastic analysis of composite structures. *Computational Materials Science*, 16:344–353, 1999.

[7] F. Feyel and J.-L. Chaboche. FE^2 multiscale approach for modelling the elastoviscoplastic behaviour of long fbre SiC/Ti composite materials. *Computer Methods in Applied Mechanics and Engineering*, 183:309–330, 2000.

[8] R. Hill. The elastic behaviour of a crystalline aggregate. *Proceedings of the Physical Society (London)*, A65:349–354, 1952.

[9] R. Hill. On constitutive macro-variables for heterogeneous solids at finite strain. *Math. Proc. Camb. Phil. Soc.*, 98(5):579–590, 1985.

[10] K. Hoffstetter, C. Hellmich, and J. Eberhardsteiner. Development and experimental validation of a continuum micromechanics model for the elasticity of wood. *European Journal of Mechanics A/Solids*, 24:1030–1053, 2005.

[11] C. Huet. Application of variational concept to size effects in elastic heterogeneous bodies. *Journal of Mechanical Physics and Solids*, 38:813–841, 1990.

[12] T.J.R. Hughes. *The Finite Element Method. Linear Static and Dynamic Finite Element Analysis*. Prentice Hall, Englewood Cliffs, N.J., 1987.

[13] T. Kanit, S. Forest, I. Galliet, V. Mounoury, and D. Jeulin. Determination of the size of the representative volume element for random composites: statistical and numerical approach. *International Journal of Solids and Structures*, 40: 3647–3679, 2003.

[14] V. Kousnetsova, W.A.M. Brekelmans, and F.T.P. Baaijens. An approach to micro-macro modeling of heterogeneous materials. *Computational Mechanics*, 27:37–48, 2001.

[15] W.M. Lai, D. Rubin, and E. Krempl. *Introduction to Continuum Mechanics 3rd Edition*. Butterworth-Heinemann, 1993.

[16] F. Maceri, M. Marino, and G. Vairo. A unified multiscale mechanical model for soft collagenous tissues with regular fiber arrangement. *Journal of Biomechanics*, 43:355–363, 2010.

[17] C. Miehe and A. Koch. Computational micro-to-macro transitions of discretized microstructures undergoing small strains. *Archive of Applied Mechanics*, 72:300–317, 2002.

[18] C. Miehe, J. Schröder, and J. Schotte. Computational homogenization analysis in finite plasticity, simulation of texture development in polycrystalline materials. *Comput. Methods Appl. Mech. Engrg*, 171:387–418, 1999.

[19] M. Ostoja-Starzewski. Material spatial randomness: From statistical to representative volume element. *Probabilistic Engineering Mechanics*, 21:112–132, 2006.

[20] Y. Pan, L. Iorga, and A. Pelegri. Numerical generation of a random chopped fiber composite RVE and its elastic properties. *Composites Science and Technology*, 68:2792–2798, 2008.

[21] D. Peric, D.D. Somer, E.A. de Souza Neto, and W.G. Dettmer. On Computational Procedures for Multi-Scale Finite Element Analysis of Inelastic Solids. In *IUTAM Symposium on Theoretical, Computational and Modelling Aspects of Inelastic Media*, 2008.

[22] B.D. Reddy and A.T. McBride. *Modeling and Simulation in Fibrous Materials: Techniques and Applications*, chapter Introduction to Finite Element Analysis (FEA) and recent developments, Chapter 1. Nova Science Publishers, Inc, New York, in press.

[23] A. Reuss. Berechnung der Fliessgrenze von Mischkristellen auf Grund der Platizitatsbedingung fur Einkristalle. *Z. angew. Math. Mech.*, 9:49–58, 1929.

[24] V. Sansalone, P. Trovalusci, and F. Cleri. Multiscale modeling of materials by a multifield approach: Microscopic stress and strain distribution in fiber-matrix composites. *Acta Materialia*, 54:3485–3492, 2006.

[25] R.J.M. Smit, W.A.M. Brekelmans, and H.E.H. Meijer. Prediction of the mechanical behaviour of nonlinear heterogeneous systems by multi-level finite element modeling. *Comput. Methods Appl. Mech. Engrg*, 155:181–192, 1998.

[26] T. Stylianopolous and V. Barocas. Volume-averaging theory for the study of the mechanics of collagen networks. *Comput. Methods Appl. Mech. Engrg*, 196: 2981–2990, 2007.

[27] I. Temizer and P. Wriggers. On the computation of the macroscopic tangent for multiscale volumetric homogenization problems. *Comput. Methods Appl. Mech. Engrg*, 198(50):495–510, 2008.

[28] I. Temizer and T.I. Zohdi. A numerical method for homogenization in non-linear elasticity. *Computational Mechanics*, 40:281–298, 2006.

[29] W. Voigt. Uber die Beziehung zwischen den beiden Elastizitatskonstanten isotoper Korper. *Wied. Ann.*, 38:573–587, 1989.

[30] P. Wriggers and M. Hain. Material Characterization based on Microstructural Computations and Homogenization. In *IUTAM Symposium on Theoretical, Computational and Modelling Aspects of Inelastic Media*, 2008.

[31] T.I. Zohdi and P.Wriggers. Aspects of the computational testing of the mechanical properties of microheterogeneous material samples. *International journal for numerical methods in engineering*, 50:2573–2599, 2001.